Summer 2019

Detecting nighttime fire combustion phase by hybrid application of visible and infrared radiation from Suomi NPP VIIRS

Sepehr Roudini
University of Iowa

DETECTING NIGHTTIME FIRE COMBUSTION PHASE BY HYBRID APPLICATION OF VISIBLE AND INFRARED RADIATION FROM SUOMI NPP VIIRS

by

Sepehr Roudini

A thesis submitted in partial fulfillment
of the requirements for the Master of Science
degree in Chemical and Biochemical Engineering in the
Graduate College of
The University of Iowa

August 2019

Thesis Supervisor: Professor Jun Wang

ACKNOWLEDGEMENTS

First, I would like to thank my academic adviser, Prof. Jun Wang, for his support and deep insights about my research topic that helped me a lot at various stages of my master project. I would like to thank my fellow friends at ARROMA group for all the discussions and the fun we have had during the past years. I especially thank Meng Zhou for helping me design the collocation algorithm, Dr. Lorena Castro Garcia for her programming support, and Dr. Xiaoguang Xu for sharing his great knowledge in satellite remote sensing of environment. Also, my sincere thanks go to my thesis committee: Dr. Greg Carmichael and Dr. Edward J. Hyer for their precious comments and suggestions about my dissertation.

Last but not the least, I would like to thank my wonderful family: my beloved wife Leyla, my devoted parents, and my brother for supporting me spiritually throughout my study at the University of Iowa and my life in general.

ABSTRACT

An accurate estimation of biomass burning emissions is in part limited by the lack of knowledge of fire burning phase (smoldering/flaming). In recent years, several fire detection products have been developed to provide information of fire radiative power (FRP), location, size, and temperature of fire pixels, but no information regarding fire burning phase is retrieved. The Day-Night band (DNB) aboard Visible Infrared Imaging Radiometer Suite (VIIRS) is sensitive to visible light from flaming fires in the night. In contrast, VIIRS 4 μm moderate resolution band #13 (M13), though capable to detect fires at all phases, has no direct sensitivity for discerning fire phase. However, the hybrid usage of VIIRS DNB and M-bands data is hampered due to their different scanning technology and spatial resolution. In this study, we present a novel method to rapidly and accurately resample DNB pixel radiances to M-band pixels' footprint that is based on DNB and M-band's respective characteristics in their onboard schemes for detector aggregation and bow-tie effect removals. Subsequently, the visible energy fraction (VEF) as an indicator of fire burning phase is introduced and is calculated as the ratio of visible light power (VLP) and FRP for each fire pixel retrieved from VIIRS 750 m active fire product. A global distribution of VEF values, and thereby the fire phase, is quantitatively obtained, showing mostly smoldering wildfires such as peatland fires (with smaller VEF values) in Indonesia, flaming wildfires (with larger VEF values) over grasslands and savannahs in sub-Sahel region, and gas fares with largest VEF values in the Middle East. VEF is highly correlated with modified combustion efficiency (MCE) for different land cover types or regions. These results together with a case study of the 2018 California Campfire show that the VEF has the potential to be an indicator of fire combustion phase for each fire pixel, appropriate for estimating emission factors at the satellite pixel level.

PUBLIC ABSTRACT

Wildfire is an uninvited fire that takes place in a wild area like a forest or a vegetated land. These fires emit into the atmosphere different amount of important greenhouse gases such as carbon dioxide (CO_2), carbon monoxide (CO), nitrous oxide (N_2O), and methane (CH_4) along with smoke particles. The emission amount of each of these gases is dependent on the fire intensity. For example, when the wildfire burns with intense flames, it emits mostly CO_2 and H_2O. In contrast, as the flaming intensity reduces, the emission of CO_2 decreases while the emission of CO increases. Hence, it is important to develop techniques to characterize the fire intensity from satellite sensors globally. In the current study, a ratio, which is fire visible energy rate over the fire total energy rate for a satellite pixel, is theoretically derived based on the physics law that shows the fire intensity.

TABLE OF CONTENTS

LIST OF TABLES

LIST OF FIGURES

CHAPTER 1. INTRODUCTION

Biomass burning has a pivotal role in Earth's atmosphere and climate system. On average 348 Mha of land is burned by wildfires and prescribed fires throughout the world each year (Giglio et al. 2013). These fires emit into the atmosphere radiatively important greenhouse gases (including their precursors) such as carbon dioxide (CO_2), carbon monoxide (CO), nitrous oxide (N_2O), and methane (CH_4) along with smoke particles like black carbon (BC) and organic carbon (OC) (Andreae and Merlet 2001; Ichoku and Ellison 2014; Ichoku and Kaufman 2005). Such greenhouse gases and smoke particles disturb atmospheric radiative balance by the scattering and absorption of solar radiation affecting climate and air quality regionally and globally (Kaufman et al. 1991; Penner et al. 1992; Ramanathan and Carmichael 2008; Wang and Christopher 2006). For example, greenhouse gases have a positive radiative forcing by absorbing the earth's longwave radiation and emitting it back to the surface, while the smoke particles can lead to radiatively cooling effect at the surface by scattering and absorbing incident solar radiation in the atmosphere.

While qualitatively understood, the overall biomass burning effects on climate and air quality are highly uncertain due to discrepancies in the estimation of biomass burning emission amount and the OC/BC ratio that regulates the single scattering albedo of the smoke particles. For example, Ge et al. (2014) conducted the WRF-Chem simulation using different OC/BC ratios in smoke emissions, and showed that the smoke direct radiative forcing increases by a factor of 2 as the OC/BC ratio changes from 10 to 3.5. Also, Feng et al. (2014) showed that the estimation for monthly-total smoke (OC + BC) emissions from 9 different inventories can differ by a factor of 12 over northern sub-Saharan Africa (15°W–42°E, 13°S–17°N). These studies highlight the importance of OC/BC ratio for both radiative forcing calculations and for resolving (at least partially) the discrepancies of the total emission of OC and BC in emission inventories.

Most emission inventories use constant emission factors (EF, grams of greenhouse gas or particulate matter emitted per kilogram burned dry matter) for each vegetation type to estimate the emissions for any wildfire. This formulation is an oversimplification because emission factors are dependent on the fire combustion efficiency (CE, the ratio of carbon emitted as CO_2 to the total carbon emitted) that in turn varies with fire combustion phase and can vary highly with space and time, even in the same region for the same surface type (Akagi et al. 2011; Reid et al. 2005). A higher value of CE (e.g., ~ 0.9) generally corresponds to the flaming phase when the biomass fuel load burns with flames emitting mostly CO_2, H_2O, and NO_X and with higher temperature BC has the ability to form. In contrast, lower values of CE, which is due to the smoldering nature of fire, results in a decrease in the emission of CO_2 accompanied by an increase in the emission of CO and OC aerosol (Ward and Hardy 1991; Yokelson et al. 1996). Hence, it is important to develop techniques to characterize the spatiotemporal variation of fire combustion phase from satellite sensors.

With the advent of polar-orbiting and geostationary satellites in the 1970s, global monitoring of fires becomes feasible. Utilizing top-of-atmosphere radiance measured in different wavelengths by satellite sensors, many fire algorithms were developed to characterize wildfires. For example, different sensors have been used to monitor fires, including Advanced Very High Resolution Radiometer (AVHRR) (Dozier 1981), the Defense Meteorological Satellite Program (DMSP) Operational Linescan System (Elvidge et al. 1996), the Along-Track Scanning Radiometer (ATSR) (Mota et al. 2006), the Visible and Infrared Scanner (VIRS) (Giglio et al. 2000), the Moderate Resolution Imaging Spectroradiometer (MODIS) (Kaufman et al. 1998), the Visible Infrared Imaging Radiometer Suite (VIIRS) (Csiszar et al. 2014; Schroeder et al. 2014), the Geostationary Operational Environmental Satellite (GOES) Imager (Prins and Menzel 1992,

1994) and the Spinning Enhanced Visible and Infrared Imager (SEVIRI) (Roberts et al. 2005; Roberts and Wooster 2008). Also, In the absence of solar contamination during the night, specific algorithms for nighttime fire detection using short-wave infrared band (SWIR) centered near 1.6 μm (Elvidge et al. 2013) and visible-light band centered near 0.7 μm (Elvidge et al. 2013; Polivka et al. 2016) were demonstrated for VIIRS onboard the Suomi National Polar-orbiting Partnership (S-NPP) satellite. The detailed specifications for each fire detection algorithm can be found in Table 1. While significant progress has been made toward detecting and characterizing active wildfires using remote sensing satellite data, there is no quantitative characterization of fire combustion phase in these satellite-based fire characterization products. The aim of this study is to develop a technique to measure fire combustion phase from space using satellite remote sensing data, thereby providing potential means to improve fire emission estimation, in particular, the emission factors for each individual fire.

Table 1. Summary of operational satellite remote sensing fire products.

Satellite	Sensor	Algorithm	Spatial Resolution (at nadir)	Spectral Channel (μm)	Main Output	Day/Night
NOAA-15 NOAA-16 NOAA-17	AVHRR	Fire Identification, Mapping and Monitoring Algorithm (FIMMA)[1]	1 km	3.7, 10.8	Fire pixel geolocation	Day & Night
Terra Aqua	MODIS	MODIS Active Fire[2]	1 km	4, 11	Fire pixel geolocation, surface background temperature, FRP	Day & Night
Suomi NPP	VIIRS	VIIRS M-Band Active Fire[3]	750 m	4, 11	Fire pixel geolocation, FRP	Day & Night
Suomi NPP	VIIRS	VIIRS I-Band Active Fire[4]	375 m	0.64, 0.86, 1.6	Fire pixel geolocation, FRP	Day & Night
Suomi NPP	VIIRS	VIIRS Nightfire[5]	750 m	1.2 1.6, 3.7, 4	Fire pixel geolocation, fire size, fire temperature, surface background temperature, FRP	Night
Meteosat Second Generation (MSG)	SEVIRI	Active Fire Monitoring (FIR)[6]	3 km	3.9, 10.8	Fire pixel geolocation, FRP	Day & Night

Table 1 - continued

GOES-13 GOES-15	GOES Imager	Wildfire Automated Biomass Burning Algorithm (WF-ABBA)[7]	4 km	3.9, 11.2	Fire pixel geolocation, fire temperature, fire size	Day & Night

[1] (Giglio et al. 1999; Li et al. 2001; Li et al. 2000); [2] (Giglio et al. 2003; Giglio et al. 2016; Justice et al. 2002); [3] (Csiszar et al. 2014); [4] (Schroeder et al. 2014); [5] (Elvidge et al. 2013); [6] (Roberts et al. 2005; Roberts and Wooster 2008); [7] (Prins and Menzel 1992, 1994)

Fire combustion phase is dependent on fuel content, relative humidity, and temperature which define the nature of combustion reaction. If the reaction happens heterogeneously at the surface of solid fuels (vegetation and wood), the combustion is without flames producing incomplete-oxidized products (Ohlemiller 1985; Rein 2009). In contrast, when the oxidation happens homogeneously between oxygen in the air and the gas pyrolyzate, combustion products are soot and complete-oxidized gases. These products absorb enough energy during the combustion process leading them to emit visible radiation as a flame (Rein 2009; Sato et al. 1969). Combustion efficiency usually reported by modified combustion efficiency (MCE) which is defined as the ratio of carbon emitted as CO_2 to the total carbon emitted as CO_2 and CO. In fire emission inventory estimates, EF is normally defined as a function of MCE. Although MCE can be identified through lab or in-situ measurements (Akagi et al. 2011; Ferek et al. 1998; Ward and Hardy 1991), it is difficult to determine MCE and therefore EF on a near real-time basis in an open-environment where both flaming and smoldering occur simultaneously (van Leeuwen and van der Werf 2011; Ward and Hardy 1991). This results in a lack of availability of MCE data for fires routinely and globally.

This study is the first attempt to use VIIRS to characterize the dominant fire combustion phase quantitatively and globally, and link that to the fire CE from which the emission factors for BC and OC can be derived for a given surface type and an individual fire. In section 2, we illustrate the VIIRS Day-Night band (DNB) and moderate-resolution band (M-band) characteristics and their spatial mismatch problem at the pixel level. In section 3, we present the development of a method to efficiently collocate DNB pixel radiances to M-band pixel resolution as DNB and M-bands have significant differences in the ways they scan. Once DNB and M-band data are homogenized, we describe the method to retrieve a variable named as visible energy fraction

(VEF) for each fire pixel, and link that to the emission factors that are used around the globe. Section 4 presents the results for different fire classifications based on their VEF values and global distribution of fire combustion phase including the first global fire combustion efficiency map for the year 2015. In the end, section 5 concludes the paper.

CHAPTER 2. VIIRS: M-BAND AND DNB SPATIAL MISMATCH AND DATA USED

VIIRS is a remote-sensing instrument flying on S-NPP and NOAA-20 (also referred to as JPSS-1). The NOAA-20 is the first in a new series of polar-orbiting environmental satellites, called the Joint Polar Satellite System or JPSS, created in partnership between the National Oceanic and Atmospheric Administration (NOAA) and National Aeronautics and Space Administration (NASA). VIIRS will be flown onboard three more satellites (JPSS-2, JPSS-3, JPSS-4) to be launched in the next 10-15 years, and VIIRS will be carried on each of these satellite platforms (Goldberg et al. 2013).

VIIRS has 22 channels with a nominal spatial resolution of 375 m in the five imagery bands (I-bands) and 750 m in 16 moderate resolution bands (M-bands), covering a spectral range from 0.412 μm to 12.01 μm (Table S1). Included on VIIRS is the unique DNB that measures radiances over a broadband spectrum from 0.4 to 0.9 μm (Cao et al. 2014; Wolfe et al. 2013). DNB minimum detectable radiance (L_{min}) is 3×10^{-9} $W\cdot cm^{-2}\cdot sr^{-1}$ during the night, which coincides with a temperature near 630 K for a fire occupying half of the pixel (Fig. 1a), to a maximum value of 0.02 $W\cdot cm^{-2}\cdot sr^{-1}$ in the presence of sunlight. Fig .1a shows atmospherically corrected DNB radiances for different fire temperatures and fractions. We assumed the night to be moonless, and did not take into account any moon effect in our simulation. The simulation was conducted by Unified Linearized Vector Radiative Transfer Model (UNL-VRTM) (Wang et al. 2014) for each fire pixel with 300k surface temperature and a uniform background aerosol optical depth around 0.1 (smoke particles). The black line represents L_{min} for the DNB. Furthermore, As Fig. 1b shows, DNB has a broad spectral response with a high dynamic range which is sensitive to the flaming fire temperatures more than 600 k. As a result of that, VIIRS DNB radiances contain strong

unsaturated signal from fire flames without major background signal contamination from the sun during nighttime.

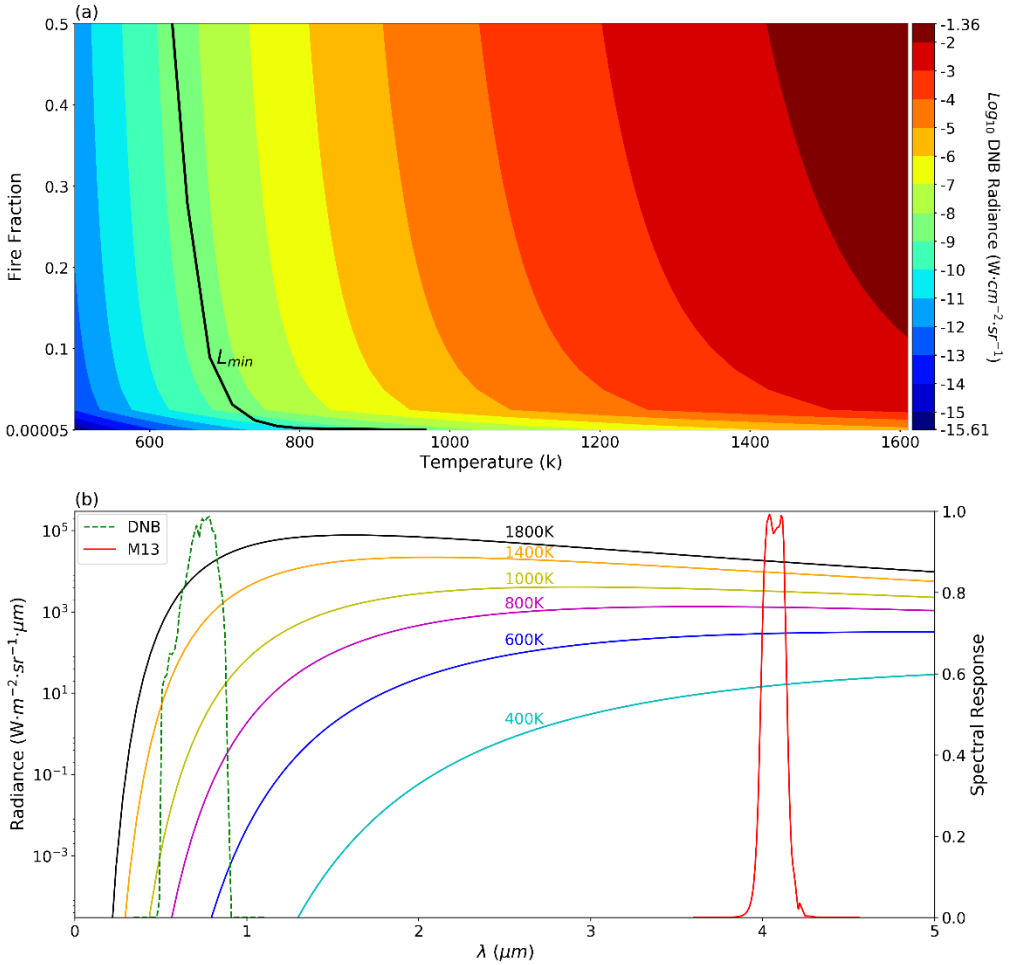

Fig. 1. (a) Contour plot of simulated DNB radiance for different fire temperatures and fractions during nighttime (moon effect is not included) using Unified Linearized Vector Radiative Transfer Model. The black line shows the minimum radiance (L_{min}) that DNB sensor can detect. The fires that fall into the left side of the white line are not detectable by DNB sensor. (b) Plot of VIIRS Day-Night band (DNB) and 4 µm moderate-resolution band #13 (M13) spectral responses along with different Plank curves for different temperatures. DNB is highly sensitive to high temperature (flaming) fires in the night while M13 is sensitive to all fire temperatures.

The VIIRS 750 m active fire (AF) product provides information on active fires and FRP. The VIIRS AF algorithm almost exclusively builds on the MODIS fire detection algorithm which is based on multi-spectral tests using the infrared channels (Giglio et al. 2016). Also, the VIIRS AF algorithm derives FRP based on the VIIRS 4 µm moderate resolution band #13 (M13) radiance

proposed by Wooster et al. (2005). However, to obtain visible light information for a fire pixel detected by infrared M-band, it is necessary to ensure that DNB pixels are properly matched to the M-band pixels. This matching is complicated by the fact that DNB and M-bands are completely different in their mechanics and operations. Subsequent sections describe these fundamental differences between DNB and M-bands in their operations to carry the observation of the earth and atmosphere and their ways to aggregate samples observed by individual detectors to form pixels. This is then followed by the description of DNB and M-band mismatch and the data products used for this study.

2.1. M-band and DNB differences in onboard processing

Each M-band has 16 detectors, and consequently, each of the M-band scans is comprised of 16 scan lines. Hereafter, the region consisting of these detector lines in one M-band scan is referred to as one scan zone. The M-bands use a whiskbroom procedure scanning the earth across the track of the satellite. (Cao et al. 2014; Polivka et al. 2015; Polivka et al. 2016; Wolfe et al. 2013). The whiskbroom scanning causes the pixel size to grow as the scan angle increases producing the so-called bow-tie effect. This pixel size growth causes some of the scan lines in two consecutive scan zones to overlap each other far from nadir, resulting in redundant sampling. For example, for the M-band, the last 9 scan lines (in order of across-scan direction) in the first scan zone overlap with the first 9 scan lines in the next scan zone, as shown in Fig. 2a. The resulting overlapped region in part is flagged onboard and removed by trimming 4 overlapped scan lines (2 from each scan zone) at the edge (corresponding to a scan angle around 56.28°) of the scan zone. However, these overlapped pixels are not completely flagged onboard and 5 more scan lines remained overlapped near the edge.

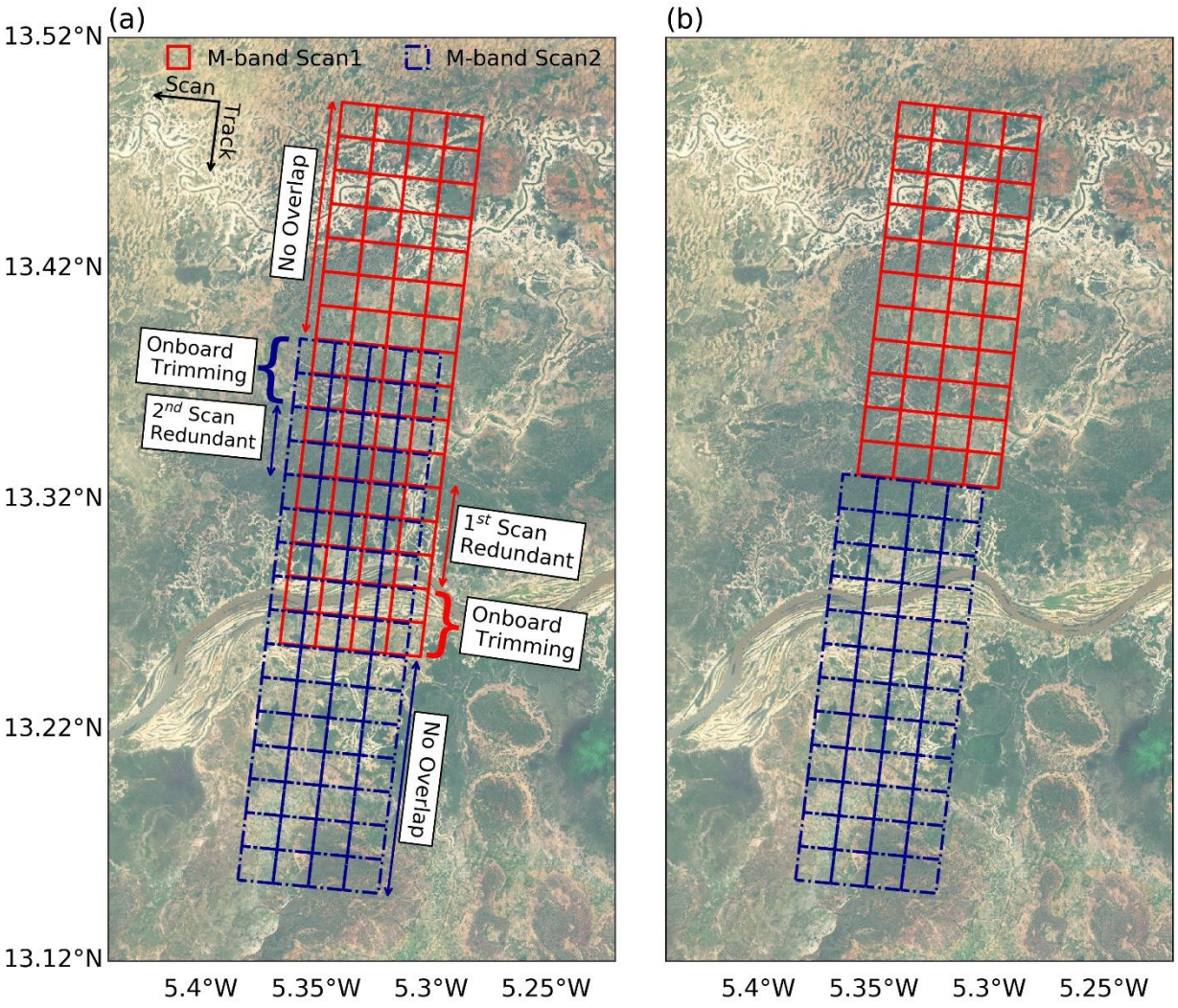

Fig. 2. View of 2 consecutive VIIRS scan zones (at the edge) overpassing Bani River in Africa. (a) Before the bow-tie effect correction there are 9 overlapped scan lines from which 4 are trimmed onboard, 2 bottommost Scan1 scan lines and 2 topmost Scan2 scan lines. The other redundant scan lines are detected using respective DNB signals which results in 3 redundant scan lines from Scan2 and 2 from Scan1. (b) Consecutive scan zones after the bow-tie effect correction.

In addition to the bow-tie effect, within each scan zone, there are three symmetrical aggregation zones for both M-band on each side of the scan zone (Table S2) (Polivka et al. 2015). Within the M-band field-of-view, each scan line has 3200 pixels after aggregation of 6304 detector pixels, and each M-band's detector samples a distance of 259 meters along the scan and 742 meters across the scan at the nadir on the earth's surface. The aggregation zones for the left side of the scan zone are denoted by blue dashed lines in Fig. 3. In aggregation zone 3:1 (scan angles between

0˚and 31.59˚), 3 consecutive samples (detector footprint) made by individual detectors along the scan are aggregated to comprise one pixel that has a size of 776 (=259×3) meters along the scan and 742 meters across the scan at the nadir. In aggregation zone 2:1 (scan angles between 31.59˚ and 44.68˚), two consecutive samples from each detector along the scan line comprise one pixel. In aggregation zone 1:1 (scan angles larger than 44.68˚), no aggregation happens as the along-scan growth in size makes each sample large enough as a square-like pixel. Without aggregation, along-scan pixel growth size is a factor of 6 of the pixel size near nadir. As a result, by aggregating 3 detector samples near nadir, along-scan pixel growth size will be a factor of 2 (instead of 6 as compared to a nadir pixel), which is the same as the growth factor across the scan (from nadir to the edge of the scan zone) , and so, the width and length of the pixel are similar throughout the scan zone.

While a similar aggregation strategy is applied, DNB uses charge-coupled device (CCD) arrays with 672 detectors across the scan (Liao et al. 2013). The large number of detectors provide the capability of aggregating small samples retrieved from detectors both along and across the scan. Contrary to M-band, DNB has 32 symmetrical aggregation schemes on each side of the scan (Table S3) to keep the similar pixel size (742 m) throughout the whole scan. In Fig. 3 the bumps in DNB lines indicate starting of a new aggregation zone which has a different number of across-scan aggregated samples than that of the adjacent aggregation zones. The unique aggregating scheme in DNB almost removes the bow-tie effect (or the pixel area overlap) completely. Consequently, DNB pixels have approximately the same size throughout the whole scan while M-band pixels are affected by the bow-tie effect.

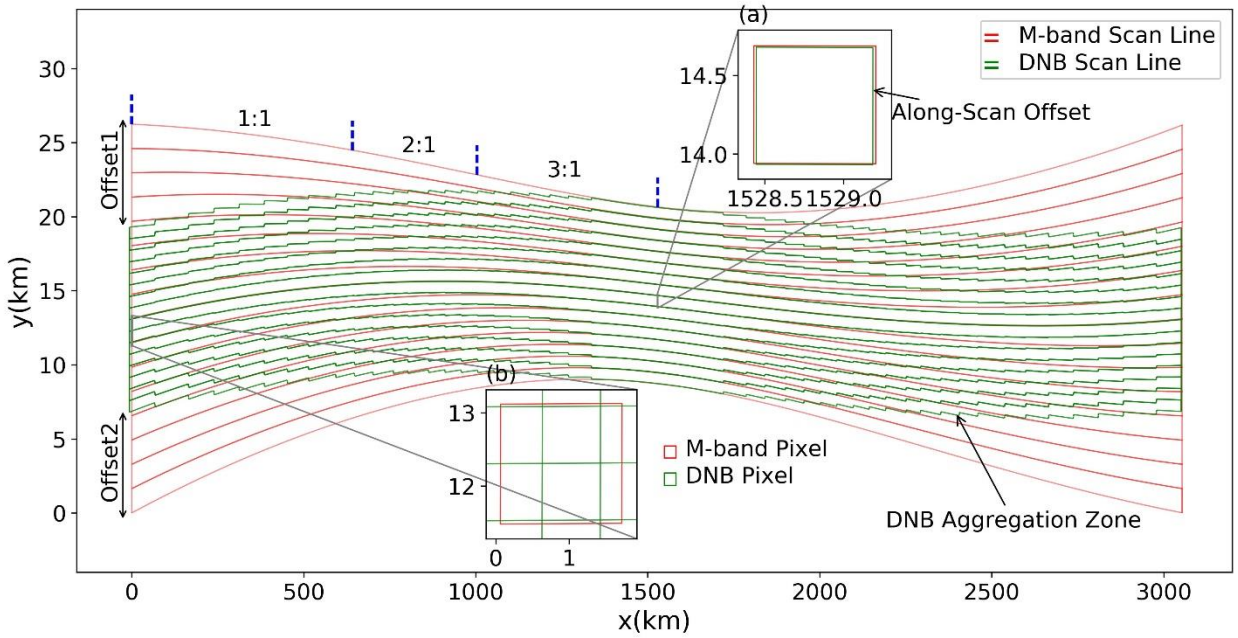

Fig. 3. VIIRS M-band/DNB scan zone for the whole swath projected on a flat plane. The DNB pixels keep the same size throughout the whole scan while the M-band pixel size grows as a function of scan angle. Near the edge, there is an offset (Offset1 & Offset2) of 8 scan lines between DNB and M-band. The bumps in the DNB scan lines indicate beginning of a new DNB aggregation zone with a different number of across-scan aggregated samples than its adjacent aggregation zones which constitutes a collocation segment. Subset. a represents the zoom-in view of the nadir M-band and DNB pixels in which the denoted along-scan empty space between M-band and DNB pixels is due to their nominal spatial resolution mismatch. Subset. b shows the zoom-in layout of the edge M-band and DNB pixels. Each large near-edge M-band pixel can overlap with up to 12 DNB pixels from 4 different DNB scan lines. Note, the different scales for X and Y axes makes the figure exaggeratedly look curvy.

2.2. M-band and DNB mismatch

As a result of the DNB and M-band on-board processing and formulation differences, two kinds of mismatch exist between VIIRS M-band and DNB pixels, even though their respective scan zone covers the same portion of the area in the VIIRS ground swath. The first type of mismatch is due to the difference between the nominal spatial resolution of the DNB and M-band pixels at nadir. As Fig. 3a shows, M-band and DNB nadir pixels match perfectly in across-scan direction (Y direction), where the top and bottom sides of the pixels overlap each other while the

left and right sides of the pixels in the along-scan (X) direction do not match exactly, rendering a small offset for the same nadir location in the same scan line.

The second kind of mismatch between M-band and DNB pixel footprints results from their different pixel size growth that in turn arises from their difference in treating the bow-tie effect. This mismatch is denoted by arrows (offset 1 and offset 2) for edge pixels in Fig. 3 where only 8 scan lines (in the center) of M-band scan zone are fully within the DNB scan zone, and fully overlap with the 16 DNB scanlines in the same DNB scan zone, while the remaining 8 scale lines of M-band are completely outside of DNB scan zone at the edge, despite having full overlap with those DNB scan lines at the nadir. Hence, an M-band pixel at the scan edge can overlap with up to 12 DNB pixels spreading over 4 adjacent DNB scan lines (Fig. 3b).

The DNB and M-band mismatch hinders the combined use of valuable DNB radiance with M-band radiances for fires that require precise georeferencing for the exact same fire area. However, since both DNB and M-band covers the same swath for the same scan zone at the nadir and their mismatch pattern is repeatable for each scan zone, it provides the opportunity to collocate DNB to M-band for one scan zone, and save the results to produce a look-up table which can be applied to any other scan zone (as described in section 3).

2.3. Data Used

We obtain the VIIRS Suomi NPP data including M-band geolocation product (VNP03MOD) and DNB geolocation product (VNP03DNB) from NASA level-1 and atmosphere archive & distribution system (LAADS) (https://ladsweb.modaps.eosdis.nasa.gov/) to implement DNB to M-band collocation. Also, We retrieve Level-1 B calibrated DNB radiance product (VNP02DNB) and VIIRS 750 m active fire (AF) product (VNP14) (Csiszar et al. 2014) from (LAADS) (https://ladsweb.modaps.eosdis.nasa.gov/) for 2017 (only nighttime). Fig. S1 in

supplementary material shows the global distribution of nighttime fire pixels for 2017. Moreover, we retrieve dominant vegetation type information from MODIS Land Cover Type Climate Modeling Grid (0.05˚) product (Short Name: MCD12C1) (Friedl et al. 2010) which is obtained from land processes distributed active archive center (LP DAAC) (https://lpdaac.usgs.gov/). MCD12C1 uses the International Geosphere-Biosphere Program (IGBP) classification stratifying the earth's surface cover into 17 categories.

We utilize gas flare location data from VIIRS Nightfire flares only product (Elvidge et al. 2016) obtained from image and data processing by NOAA's national geophysical data center (https://ngdc.noaa.gov/) to classify flare-type grids. Fig. S2 in supplementary material shows the gas flare locations that are used in this study.

We use global fire emissions database version4 (GFED4) (https://www.globalfiredata.org/) (van der Werf et al. 2017) data to calculate MCE ($= \frac{CO_2}{CO_2+CO}$) for each GFED4 grid (0.25˚) which is used as a check for the results. GFED4 reports monthly emission estimation (grams) of different trace gases like CO and CO_2 for different vegetation types for the globe. It also provides these estimations for 14 basis regions.

2.4. Data Processing

We extract FRP data from VIIRS AF for all the detected nighttime (having a solar zenith angle greater than 85˚) fire pixels for 2015 and 2017 globally. Also, we repeat the analysis including only fire pixels with a confidence level more than 50%, and the results are almost identical. Consequently, we include all the fire pixels in our analysis. Then, we use the collocation algorithm to obtain the collocated DNB radiance and, calculate VEF for each of those (M-band) fire pixels. We regrid the pixels into different grid resolution according to the application. For

example, for characterizing VEF for different surface cover types we regrid VEF pixel data into MODIS land cover type grids (0.05˚), for comparison purposes we use GFED4 grids (0.25˚) to compare VEF with MCE, and finally, we regrid VEF pixel values into 1˚ grids to show a global map of VEF. We only use the grids with at least 5 fire pixels and report annual-averaged VEF for each grid by averaging pixel VEF values in each grid.

We employ VEF to investigate the nighttime fire combustion phase based on the different MODIS IGBP land cover types (Fig. 9b, Table 2) and gas flares (Fig. S2). Note, we consider MODIS savannas and woody savannas as one land cover type (savannas), and open/closed shrublands as simply shrublands. Furthermore, we show VEF capability to characterize fire combustion phase by correlating it to the MCE values derived from GFED4 2015 emission data for 14 GFED4 basic regions (Fig. 4a) as well as 6 GFED4 general biomes plus the gas flares (we assume gas flaring MCE to be 0.99 as the gas flares are mostly comprised of flames). For that purpose, we reclassify the MODIS land cover types into the broad vegetation types that are used by GFED4 for reporting emission factors (Akagi et al. 2011) and dry matter emissions (Table 2). In this way, we can compare and correlate VEF and MCE for the same biomes. However, MODIS land cover product does not provide peatlands locations while peat is one of the biomes used by GFED4. As a result, we find the peatland grids by deriving the fraction of peat vegetation for each GFED4 grid (0.25˚); if more than 70% of a grid land cover is peat, we classify it as peatlands which are located at regions of Sumatra and Kalimantan (Fig. 4b). However, in 2017 there were not enough fire pixels in these peatland grids resulting in inadequate VEF information for peats. Consequently, we use the 2015 VIIRS AF data because of the large peatland fire incident which happened in Indonesia (Huijnen et al. 2016) providing us with enough valid peatland grids so that

we can retrieve a reliable VEF for peat vegetation type. Finally, we illustrate how VEF can show the wildfire intensity changes during its lifetime by analyzing wildfire Camp Fire.

Table 2. MODIS land covers reassigned to more general vegetation types as in GFED4.

MODIS Land Cover Type	Clustered Vegetation Type
Evergreen needleleaf forest (ENF)	Tropical, Temperate, Boreal[1]
Evergreen broadleaf forest (EBF)	Tropical, Temperate, Boreal
Deciduous needleleaf forest (DNF)	Tropical, Temperate, Boreal
Deciduous broadleaf forest (DBF)	Tropical, Temperate, Boreal
Mixed forest (MF)	Tropical, Temperate, Boreal
Closed shrublands (Shrub)	Savanna
Open shrublands (Shrub)	Savanna
Woody savannas (Sava)	Savanna
Savannas (Sava)	Savanna
Grasslands (Grass)	Savanna
Croplands (Crop)	Agricultural

[1] If latitude between 30N and 30 S: Tropical, if latitude between 30N/S and 50N/S: Temperate, and if latitude larger than 50N: Boreal

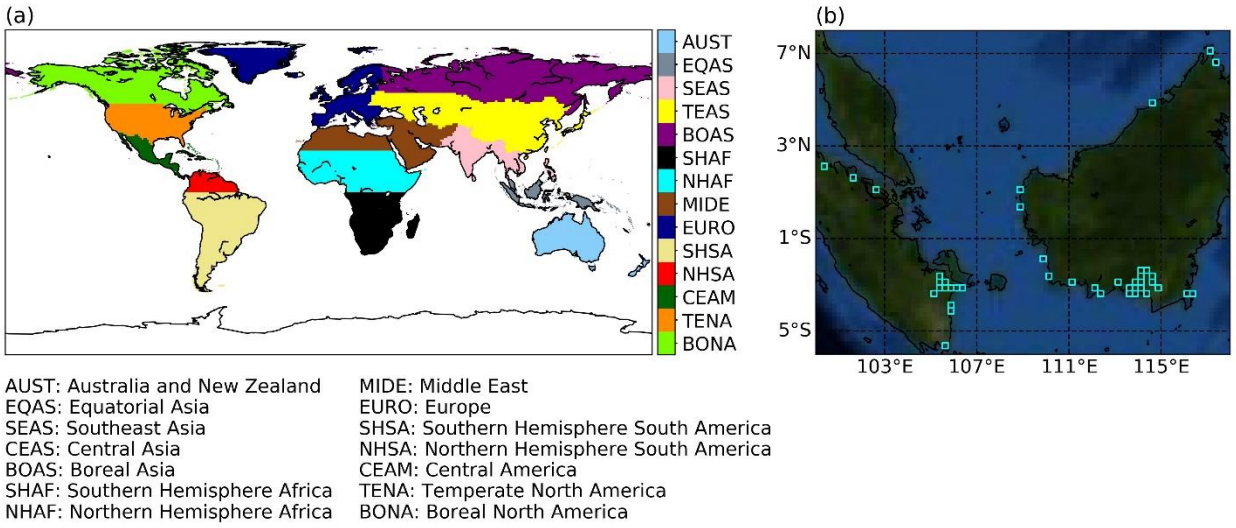

Fig. 4. (a) Map of 14 basic regions used by GFED. (b) Peatland locations in cyan-colored boxes used in this study. Each grid land cover is comprised mostly from peats (70%). The background base map is from ESRI (Environmental Systems Research Institute) world imagery service.

CHAPTER 3. ALGORITHM

3.1. Collocating DNB to M-band

The principle of collocation is to aggregate different DNB pixels into M-band resolution by assigning them different weights according to their respective area and the corresponding M-band pixel area. We collocate DNB to M-band for a scan using area-weighting, so the energy is conserved in the collocation process. We choose a scan specifically near the equator that has minimal curvature effect to reduce errors in calculating areas of pixels. The collocation process is summarized as a flow chart in Fig. 5.

For the first step in the colocation algorithm, we split up one scan zone of DNB in the along-scan direction (X-axis) into smaller segments called collocation segments, so that we can implement the collocation process for each of these small segments separately to reduce distortion errors. We use the DNB aggregation zones as our index for collocation segments. If two consecutive aggregation zones have the same number of across-scan aggregating detector samples (as described in section 2.1), they will be assumed as a single collocating segment because the pattern along the scan will remain consistent (Fig. 3). There are 64 aggregation zones for one DNB scan zone (32 on each side of nadir) which comprises 46 collocation segments (23 on each side). The details of the pixel ranges for each collocation segments are provided in Table S4 in the supplementary material.

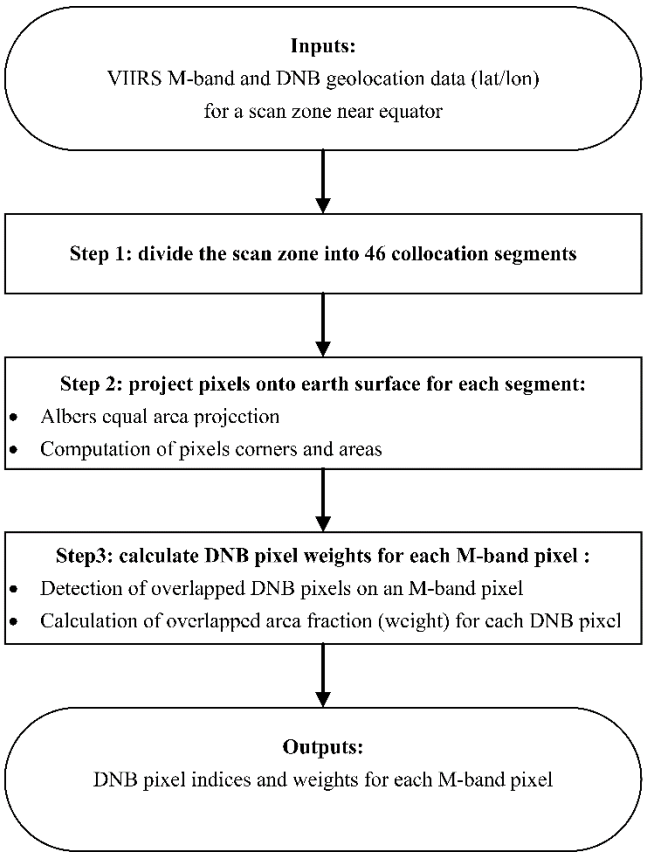

Fig. 5. Flowchart demonstrating the collocation process.

Second, for each collocation segment, pixels are projected onto the earth's surface and the projected pixels centroids are used to calculate each pixel corners and area. Albers equal area projection method is used to project pixel lat/lon coordinates to a flat surface because it is appropriate for satellite swath data as the distortion is minimal in east to west direction in the scan zone (Yildirim and Kaya 2008). This flat surface is a two-dimensional coordinate system where the horizontal axis (X-axis) corresponds to the projected longitude and the vertical axis (Y-axis) represents the projected latitudes in meters. The origin point (X=0, Y=0) of the flat surface corresponds to the lower left pixel in the collocating segment. Fig. S3 shows the projected DNB and M-band pixels comprising collocation segment 7.

In the third step of the algorithm, for each M-band pixel in the scan zone of DNB, the overlapped DNB pixels for each M-band pixel are identified, and their area weights are calculated. This step will be applied to all M-band pixels in each collocation segment. Then, we calculate the weight of each intersecting DNB pixel. We denote the given M-band pixel as $M_{i,j}$ where the subscript i shows the scan line (from 1 to 16) and j is the number of pixels along that scan line (from 1 at nadir to 3200 at edge). Similarly, a DNB pixel is denoted as $D_{l,k}$ where l is the scan line (from 1 to 16) and k is the pixel number (from 1 to 4064). As shown in Fig. 6, x_{MLR} and x_{DLR} represents the pixel lower-right X coordinates (along X axis) of respectively $M_{i,j}$ and $D_{l,k}$ on the earth along the scan in meters while x_{MLL} and x_{DLL} are the lower-left X coordinates along the scan. Similarly, y_{MUL} and y_{DUL} are the upper-left Y coordinates (along Y axis) of respectively $M_{i,j}$ and $D_{l,k}$ across the scan in meters whilst y_{MLL} and y_{DLL} are the lower-left coordinates of each pixel. The $D_{l,k}$ is intersected with $M_{i,j}$ if:

$$\Delta X = Min(x_{MLR}, x_{DLR}) - Max(x_{MLL}, x_{DLL}) > 0 \quad (1)$$

$$\Delta Y = Min(y_{MUL}, y_{DUL}) - Max(y_{MLL}, y_{DLL}) > 0 \quad (2)$$

Where the minimum of the two coordinates denotes the smaller value of those while maximum means the larger coordinate value. Once the intersection is detected, the ratio of the intersected area of DNB pixel to M-band pixel area, which is the area weight, is calculated as follows:

$$S_{i,j}^{M} = (x_{MLR} - x_{MLL}) \times (y_{MUL} - y_{MLL}) \quad (3)$$

$$S(D_{l,k}, M_{i,j}) = \Delta X \times \Delta Y \quad (4)$$

$$W(D_{l,k}, M_{i,j}) = \frac{S(D_{l,k}, M_{i,j})}{S_{i,j}^{M}} \quad (5)$$

Where $S_{i,j}^{M}$ is the $M_{i,j}$ pixel area and S ($D_{l,k}$, $M_{i,j}$) is the area that $D_{l,k}$ intersected with $M_{i,j}$. The weight of $D_{l,k}$ for $M_{i,j}$ is denoted by W ($D_{l,k}$, $M_{i,j}$). After we calculate the DNB area weights, the collocated DNB radiance can be calculated as follows:

$$R_{M_{i,j}}^{D} = \sum_{l,k} W\ (D_{l,k}\ , M_{i,j}\ ) \times R_{l,k}^{D} \tag{6}$$

Where $R_{M_{i,j}}^{D}$ is the DNB radiance for $M_{i,j}$ and $R_{l,k}^{D}$ is the radiance retrieved from the intersected DNB pixel ($D_{l,k}$). It should be noted that the sum of the intersected DNB pixels weights will add up to 1 ($\sum_{l,k} W\ (D_{l,k}\ , M_{i,j}\ ) = 1$) for each $M_{i,j}$ that is completely overlapped with DNB pixels.

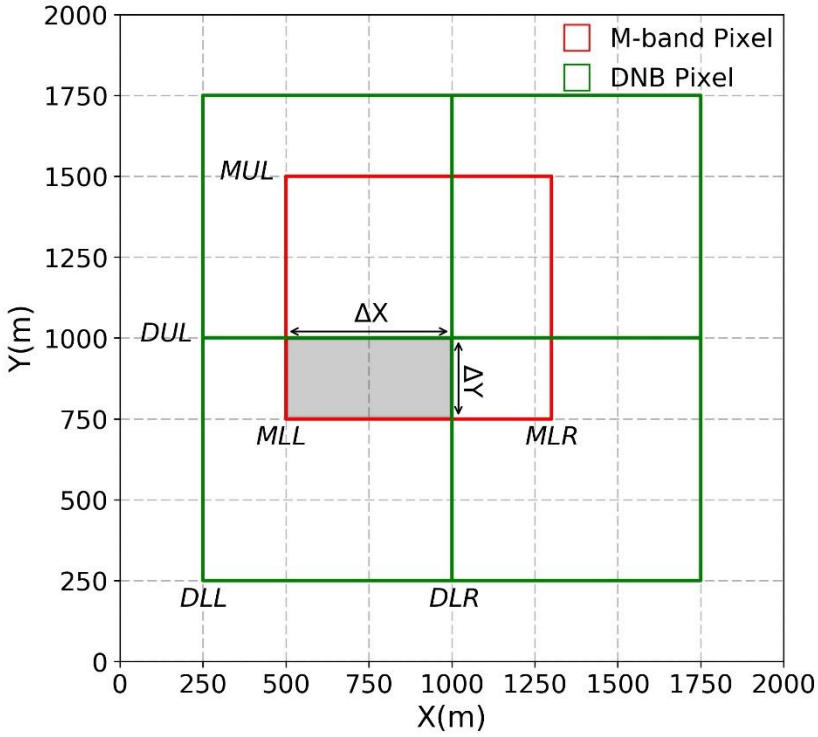

Fig. 6. Detecting intersection area between M-band and DNB pixel. The two pixels are overlapped if $(x_{DLR} - x_{MLL})$ *and* $(y_{DUL} - y_{MLL})$ are simultaneously larger than zero. Subscripts of *DLL*, *DLR*, *DUL*, *MLL*, *MLR*, and *MUL* stand for DNB lower left, DNB lower right, DNB upper left, M-band lower left, M-band lower right, and M-band upper left respectively. The X axis corresponds to projected longitudes while Y axes represent projected latitudes.

We store the index of each M-band pixel and its corresponding intersected DNB pixels indices and weights as a collocation look-up table (LUT). Also, we add the M-band pixel areas to

the pixel-area LUT for later use. The collocation LUT details are presented in supplementary material section 1. These LUTs can be applied to any other scan zone because satellite scan zone characteristics, such as pixels areas or pixel size growth pattern are inherent and do not change for different scan zones. For example, a near-equator scan zone's pixels areas are nearly identical for a scan zone in Polar Regions. Furthermore, the area-weighted collocation method can be applied to any other data with different spatial footprints which need to be resampled to each other. The resampling process for an M-band granule (consists of 3232 scan lines) by applying collocation LUT takes around 3 seconds (using an inexpensive laptop) while it can take up to hours implementing the resampling process without using LUT. The resampled DNB radiances for M-band pixels give us the capability to characterize fire combustion efficiency for each nighttime fire pixel.

3.2. M-band bow-tie effect and pixel overlap removal

We detect M-band bow-tie affected pixels that are overlapped on each other from two consecutive scan zones using the same technique described in section 3.1. We use 50% as the threshold for detecting the overlap; if the two M-band pixels overlap more than 50% of their area, they are labeled as overlapped. Still, it is not clear to remove which of the two overlapped pixels as redundant. We use weights of DNB to decide which pixel is redundant. We sum up the DNB weights for each overlapped M-band pixel and remove the M-band pixels that have minimum values from corresponding DNB pixels in the same scan zone. For example, near the edge, we detect 9 scan lines to be overlapped between two consecutive scans (Fig. 2a). According to the edge offset (Offset1 & Offset2) of 8 scan lines between DNB and M-band, the last 4 lines from the scan zone 1 and the first 4 lines from the second scan zone has no DNB pixel overlap; hence they are labeled as redundant pixels (Fig. 2a). Similarly, although the last overlapped line between

two scan zones has DNB signals from both scan zones, the DNB weights from the first scan zone are larger than second scan zone which results in labeling one more scan line from scan zone 2 as redundant. As a result, we remove the 4 bottommost scan lines from scan zone 1 and the 5 topmost scan lines from scan zone 2 as the redundant pixels (Fig. 2b). We detect all the overlapped pixels along the whole scan zone for two consecutive scans, and store the results as a bow-tie look-up table.

3.3. Visible Energy Fraction (VEF)

Polivka et al. (2016) showed that VIIRS DNB radiance in the night time can be an indicator of fire combustion phase of smoldering versus flaming. However, no quantitative measurement was presented to quantify the CE. Considering the fact that the VIIRS active fire (AF) product provides near real-time fire radiative power (FRP), is an estimate of instantaneous radiative energy from actively burning fires (Csiszar et al. 2014; Kaufman et al. 1998; Peterson et al. 2013; Wooster et al. 2005) for each fire pixel, we derive visible energy fraction (VEF) to quantitatively measure the flaming/smoldering phase for each fire pixel. VEF of a fire is defined as the ratio of its visible light power (VLP) to FRP. The visible energy rate for each fire pixel is calculated as follows:

$$VLP = L_{visible} \times A_{pixel} \times \pi \times 10^{-6} \quad (7)$$

Where VLP (in megawatts) is the fire pixel visible energy , $L_{visible}$ (in $W \cdot cm^{-2} \cdot sr^{-1}$) is the collocated visible radiance from the fire ($R^{D}_{M_{i,j}}$), A_{pixel} (in cm^2) is the M-band pixel area, π is a mathematical constant approximately equals to 3. 14 (in steradians), and 10^{-6} is the unit conversion factor from Watts to megawatts. It should be noted that $L_{visible}$ is not corrected for background contamination (e.g. city lights) or moonlight. For example, the presence of intensive city lights in a fire pixel can result in overestimation of fire radiance. However, most of the wildfires happen in

remote areas with almost no background contamination ($L_{visible} \approx 0$). Also, the radiance from a full-moon do not exceed 10 nW·cm^{-2}·sr^{-1} (Román et al. 2018) which is comparable to $L_{visible}$ of only around 3% of 2017 fire pixels (If we assume that all the fire pixels are under full moon condition). Once the VLP is obtained for the pixel, VEF can be calculated as follow:

$$VEF = \frac{VLP}{FRP} \tag{8}$$

where FRP (in megawatts) is the fire radiative power for the fire pixel. The major uncertainty source for VEF is heavy smoke plumes. Light is more extinct and scattered in the visible spectrum (e.g. 0.7 μm) than infrared (e.g. 4 μm). Consequently, VLP is more affected than FRP which means the VEF ratio suffers from underestimation under heavy smoke conditions. We simulate VEF using UNL-VRTM for different fire temperatures (Table S5) and a smoke optical depth around 0.1. We compare the simulated VEF with the 2017 fire pixels VEF values to determine the approximate dynamic range for VEF. For example, the maximum VEF value (≈ 0.25) in our data belongs to gas flare pixels which is close to the simulated VEF value (≈0.28) for a temperature of 2400 k. Also, we find out that the minimum VEF value ($\approx 2.9 \times 10^{-9}$) in 2017 fire pixels corresponds to a temperature around 570 k in simulation. This temperature, though different, is somewhat near the minimum detectable fire temperatures by DNB.

CHAPTER 4. RESULTS AND DISCUSSIONS

4.1. Resampling DNB radiance to M-band footprint

Fig. 7 a & b show a case of resampling DNB radiances into the M-band pixel resolution by applying the collocation LUT. Before the collocation, the bright DNB radiances distinguishes them from the larger M-band pixel footprint (red rectangles). These pixels are retrieved by VIIRS on 12 December 2017 (10:24 am UTC) over California where the Thomas wildfire took place. After collocating the DNB radiances based on their respective areas intersected with the M-band pixel footprint, the bright DNB pixels are smoothed over the M-band pixel area which indicates conservation of energy over the area as a result of the area-weighting resampling (Fig. 7b).

Also, to illustrate the effectiveness, we compare our collocation method results with the nearest-neighbor method, which is highly used for collocation processes in satellite remote sensing data, by correlating collocated DNB radiances to the brightness temperature values for 852 nighttime fire pixels (Thomas fire) detected by VIIRS AF from 5 December to 12 January 2017 (note the data are at log scale). Fig. 7c shows when the collocation is only based on the nearest pixel method (i.e. the nearest DNB pixels to an M-band pixel in the same scan line are remapped to M-band footprint), the resampled radiances do not show a promising correlation (R=0.21) with the corresponding 4 μm brightness temperature (BT_4) values while when the collocation LUT method is applied, the collocated radiances are more reliable and well correlated (R=0.61) with the M-band pixels BT_4^4 (the fire pixel energy) values (Fig. 7d).

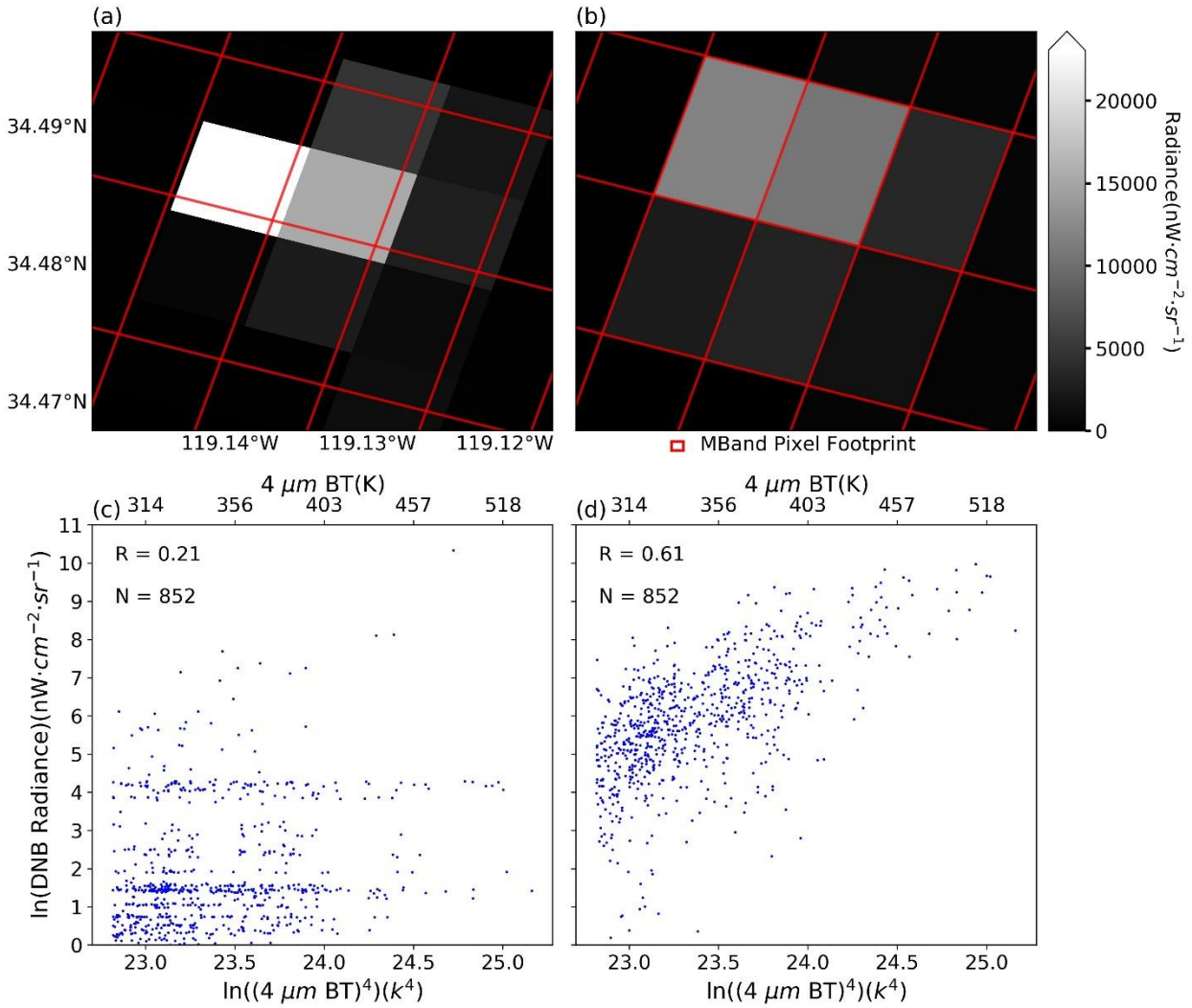

Fig. 7. An example of resampling nighttime DNB pixels radiances to M-band pixels using collocation LUT method for Thomas wildfire on December 12, 2017. (a) Zoom-in view of the original DNB radiances (bright squares) before the collocation. (b) The DNB radiances after collocation to the M-band footprint (red rectangles). (c) Scatter plot of BT_4^4 and collocated DNB radiances for VIIRS AF (nighttime) fire pixels (Thomas wildfire) during the December 5 to January 12, 2017 period when only the nearest DNB pixels in each scan line are collocated to the M-band pixel footprint without considering the across-scan offset. The low correlation coefficient indicates the low accuracy of the nearest-neighbor collocation method. (d) Same as Fig. 7c, but here the collocation LUT method results in a high correlation between the collocated DNB radiances (both across and along the scan) and the corresponding M-band pixel BT_4^4 values.

4.2. Fire combustion phase based on the VEF

Each vegetation type follows a specific combustion phase (smoldering/flaming or a mixture of them) based on its chemical compound, fuel content, relative humidity, and fire temperature. As Fig. 8a shows, although almost all fire types have a similar FRP range, their VEF ranges are different from each other which indicates that VEF can successfully characterize different fire combustion phases (note that each point VEF and FRP is an annual-averaged value for a 0.05˚ grid for 2017). It is because FRP represents the power of the fire which is dependent on the fire size and intensity. For instance, FRP is the same for a large smoldering fire and a small intense flaming fire (Peterson et al. 2013). Hence, FRP is not capable of detecting fire combustion phase, while VEF is a ratio unique for each fire pixel representing its combustion phase. For example, our results show gas flares VEF values are clustered on the top of all the other fire types which is expected as they consist of pure flames. Furthermore, Fig. 8a shows that all the forest land cover types have smaller VEF comparing to savanna, grassland and shrubland indicating they have a smaller MCE which is consistent with the literature (Reid et al. 2005). In Fig 8b, we show the VEF and FRP distributions for only three fire types to better visualize and illustrate that although, each of the gas flare, shrubland and evergreen broadleaf forest fire types are clustered in a specific range different than others, they still can be highly variable in that range because even if for the same vegetation type, the fire combustion phase still can vary due to the differences in the fire temperature and relative humidity. This interesting result indicates that VEF has the potential to in part describe the variation of fire combustion phase by each fire pixel

We show the ln(VEF) probability density function (PDF) for each of the fire types in the fig. 8c. Note, We also plot the not-averaged data, and the results are almost identical (Fig. S4). Shrubland, grassland, and cropland are spread over a similar ln(VEF) range. The average of VEF

values for each MODIS land cover type are shown in Table S6. Shrubland fire type, for example, is more flaming as its PDF has a peak in a larger ln (VEF) than the other two fire types. Savanna's PDF covers a wide range with a peak around -7 (corresponds to a VEF value of 0.00091). It has a longer tail on the left side of its peak meaning that it has more fires in the smoldering phase comparing to Shrubland. The forest fires PDFs ranges are lower comparing to other fire types because the forests generally burn with less MCE comparing to shrublands or grasslands. Mixed forest fires have a larger peak comparing to the other forest fires peaks. Also, mixed forest has a small peak around -5 (corresponds to a VEF value of 0.0067) which is very high and indicates a dominant flaming fire phase. Finally, gas flares are mostly located over the highest range from -5.5 to -3.5 which is consistent with the fact that they have dominant flaming combustion.

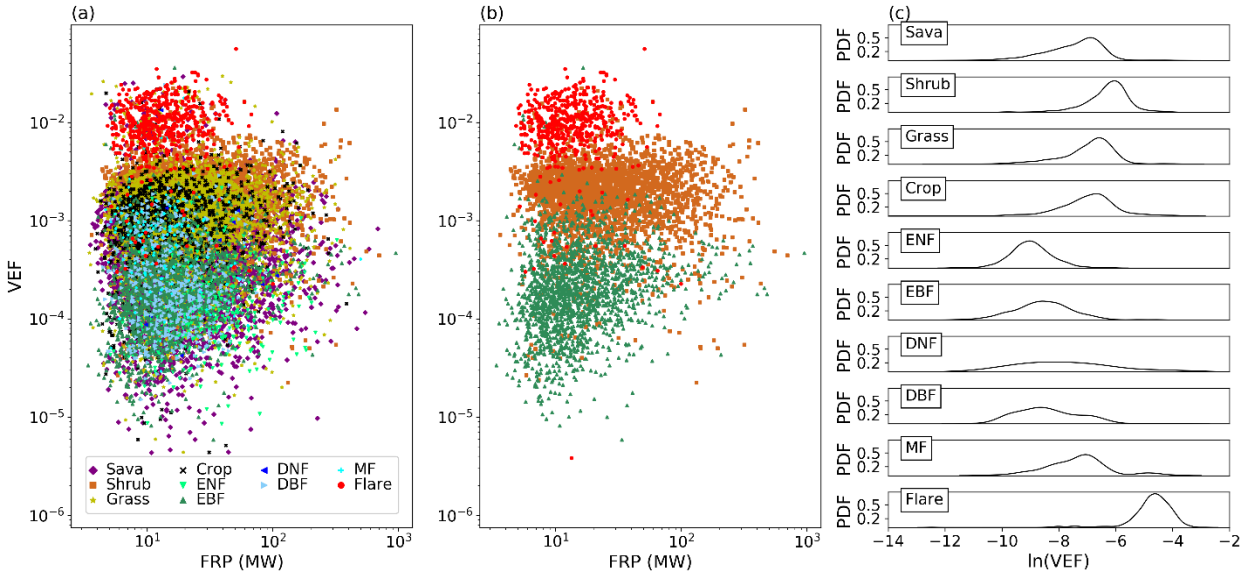

Fig. 8. (a) Scatter plot of different fire types VEF and FRP values. The fire types are based on the different vegetation types (Table 2) plus gas flares. Each point on the scatter plot represent a 0.05˚ grid average VEF (y-axis) and FRP (x-axis) values for 2017 (only nighttime). Different fire types are clustered by their VEF value ranges while they have a similar FRP range. (b) Same as Fig. 9a, but here only three fire types are presented for better visualization. Gas flares have the highest VEF range while EBF has the lowest VEF clustered under the shrublands. (c) The probability density functions (PDF) for different vegetation types showing their VEF distribution for the year 2017. Sava, shrub, grass, and crop ln(VEF) values are mostly distributed from -8 to -5 while different forest types are from -10 to -7 and gas flares are mostly spread in the highest range from -6 to -3.

4.3. VEF Global Distribution

Fig. 9a shows a global map of averaged nighttime VEF (1˚grids) for 2017. Also, we show the MODIS Global landcover map to better visualize the relationship between land cover types and the VEF (Fig. 9c). Note, we replot the global maps at a 0.25˚grid level which yield similar results comparing to maps at 1˚grid level (Fig. S5). We see from the VEF map that the savanna regions in Middle America (Consists of Mexico, Central America, Caribbean, Columbia, and Venezuela) have lower VEF comparing to Africa savanna which means that they are included in the left tail of savanna's PDF (Fig. 9c). Furthermore, according to Fig. 9a zoomed-in subplots, open shrublands in Australia burn mostly with a flaming phase as they have high VEF values which distinguish them from evergreen needleleaf forest type in North America with low VEF values indicating the smoldering type. In general, it is apparent from the map that the forest land covers, regardless of the type, have a lower VEF in comparison to savannas, shrublands, grasslands, and croplands. For example, in South America, the VEF changes from high values to smaller values as biomes transit from grasslands and savannas to evergreen broadleaf forests. The same scenario is seen in Australia, North America, and Africa. Also, the red grids that have the highest VEF are mostly corresponding to the gas flares in Middle East, North Africa, Russia, and Mexico. In contrast to the VEF, global map of nighttime averaged FRP (1˚grids) (Fig. 9b) is not showing the transitions between different fire types clearly. For example, gas flares are not detectable as their FRP range is similar to the other fire types, or as the zoomed-in subplots show, the FRP spread is similar for Shrublands in Australia and evergreen needleleaf forest in North America while the two land cover types are very different. This indicates that, as expected, the main driver of the mean-state VEF for each grid is VLP (Fig. S6). However, zoomed-in subplots in Fig. S6 shows that the gas flares are better separated from shrublands in the VEF map because

unlike VLP, VEF is not driven by the fire size. For example, Fig. S7 in supplementary material shows cases of fire pixels with large VEF values (e.g. more than 0.2), but not large VLP values. We found out that these fires pixels correspond to gas flares in Venezuela indicating that VEF can rigorously distinguish between small fires with intense flaming combustion phase and large fires with smoldering combustion phase.

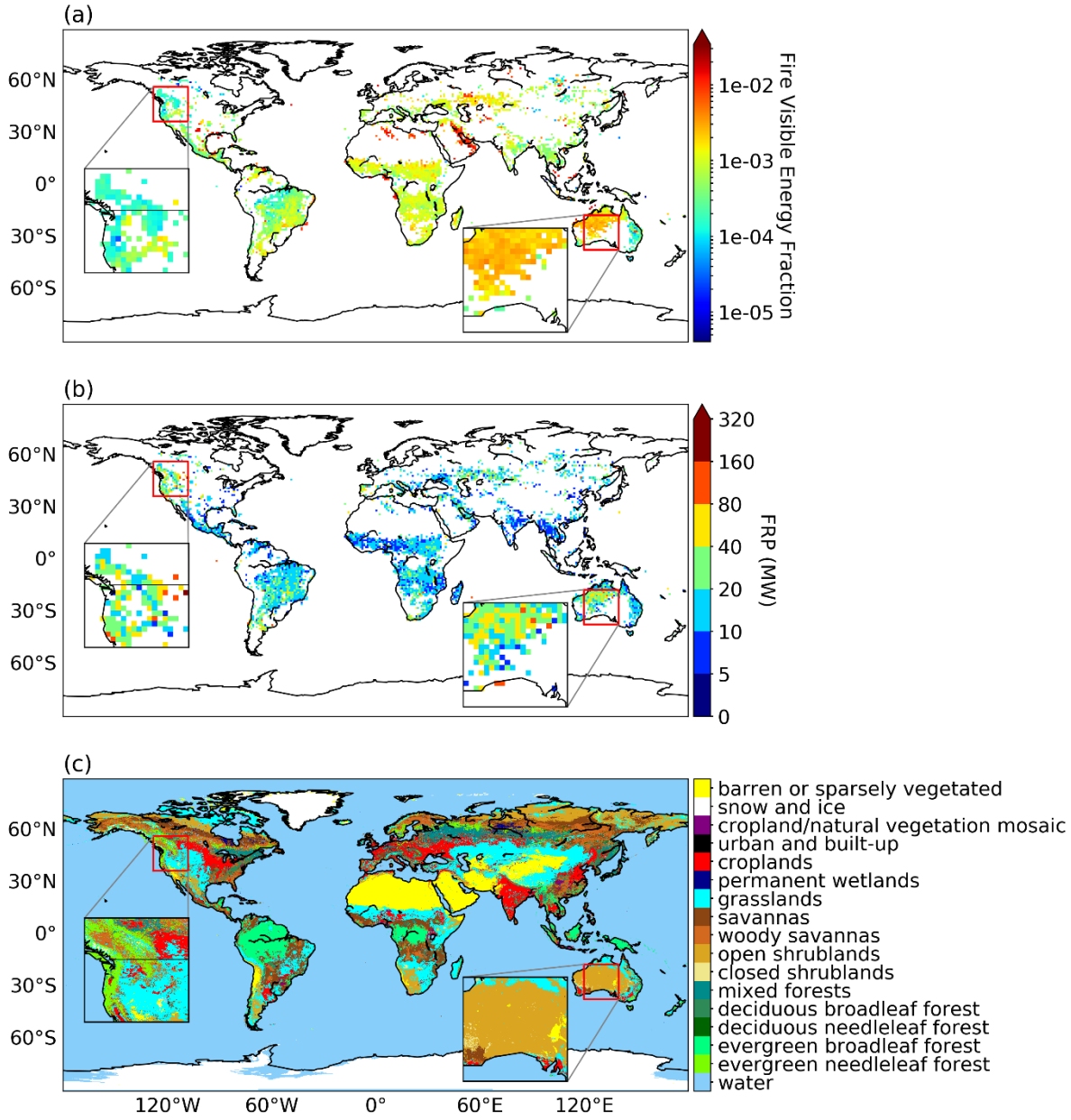

Fig. 9. (a) Global map of VEF for 2017. Each 1˚ grid represents the average VEF value for the year 2017. The VEF map shows the transition from forest land cover type in North America (lower VEF) to shrublands in Australia (higher VEF). The red grids (highest VEF) are mostly corresponding to the gas flares while the lowest VEF (blue color) are where the evergreen forests are. There are no detected nighttime fire pixels in polar regions including Greenland and Alaska due to the long day length (more than 20 hours) during their fire seasons in summer. (b) Global map of FRP for 2017. Each 1˚ grid represents the average nighttime FRP value for the year 2017. The FRP map is not capturing the fire combustion phase differences based on the land cover type as the FRP spread for shrubland and forest are similar. (c) Global landcover map generated based on the MODIS Land Cover Type Climate Modeling Grid for the year 2017. The land cover categories are according to IGBP scheme.

4.4. VEF Comparison with MCE

Although VEF is available for each nighttime fire pixel individually, there are limited in-situ measurement data, which coincide with the VIIRS overpass, to compare our VEF values with MCE on a pixel level. As a result, we use GFED4 data which provides emission estimations of CO and CO_2 at a resolution of 0.25˚. However, the GFED grid-based MCE is derived based on both day and night fire data, which leads us to derive annual-averaged VEF and MCE to obtain a mean-state of each land cover type/region. We calculated annual-averaged VEF for different surface types for 2015 and compare with their MCE values derived from GFED4. We show that ln(VEF) is highly correlated (R=0.89) with MCE for different biomes (Fig. 10a). Furthermore, Fig. 10b shows that the regional averaged VEF and MCE are correlated with each other confirming the strength of VEF in capturing the fire combustion phase. These results suggest that VEF is a strong indicator for fire MCE based on the fire type and combustion conditions (e.g. relative humidity). In other words, GFED-based MCE can be estimated for each nighttime fire pixel on a near real-time basis by taking advantage of its linear relationship with VEF:

$$MCE = 0.016 \times \ln(VEF) + 1.061 \quad (9)$$

However, it should be noted that the MCE calculated from equation 9 includes errors/uncertainties from both GFED and VEF sources, and it is simply a step forward towards improving emission estimations on a near real-time basis.

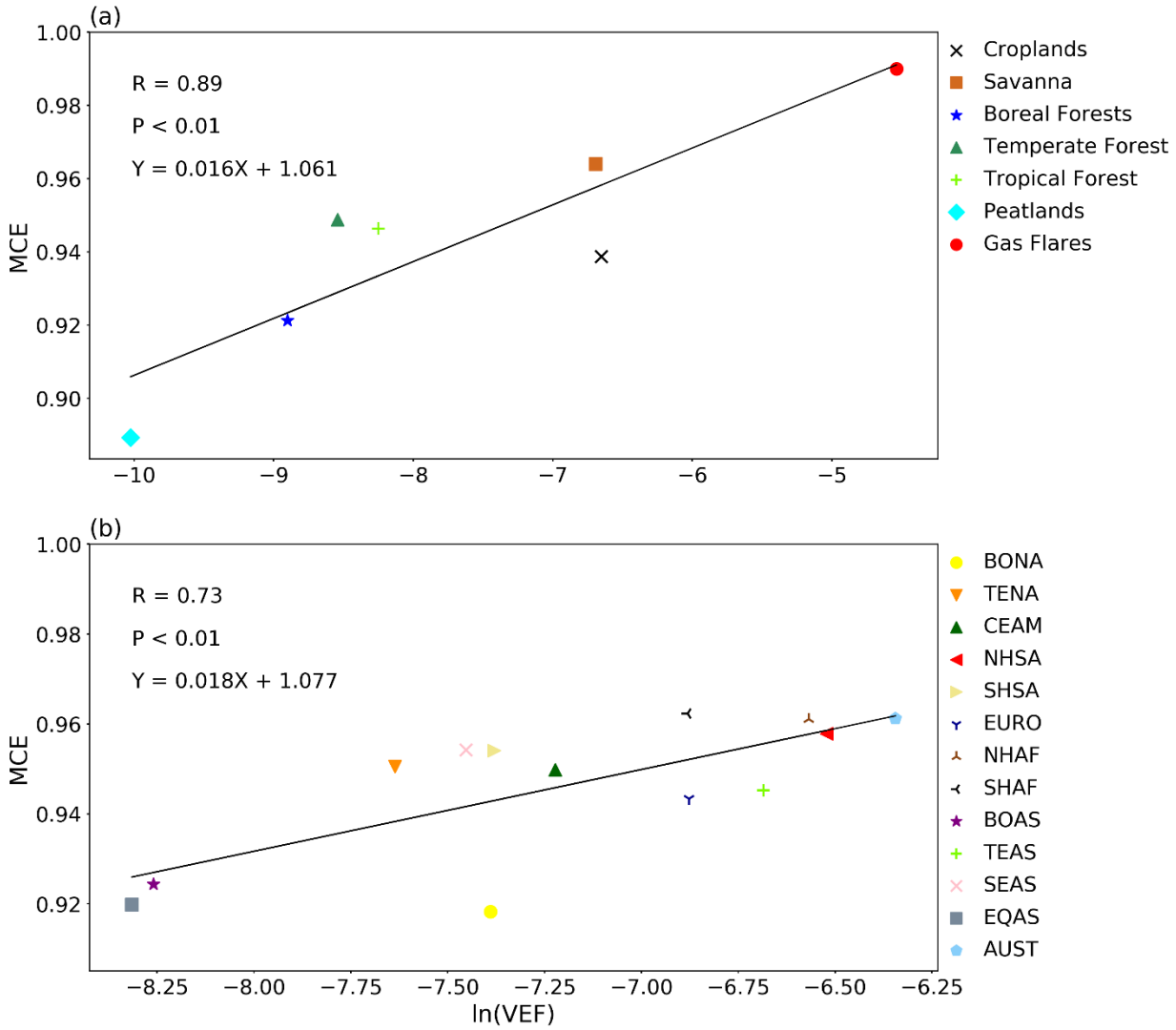

Fig. 10. (a) Scatter plot of annual-averaged (2017) GFED4 MCE and ln(VEF) for different biomes. Correlation coefficient is 0.92 indicating VEF is a successful indicator of fire combustion phase for different biomes. (b) Scatter plot representing the regional MCE and VEF relationship. Each point represents GFED4 MCE (y-axis) and the natural logarithm of VEF (x-axis) averaged for a GFED4 basic region during 2015.

Fig. 11 shows the global map of MCE for 2017. Each grid value computed from the pixel VEF values linked to the MCE by equation 9. As expected, gas flares have the highest MCE while the forest land cover types have the lowest values. The same approach can be applied to each pixel VEF and once MCE is calculated for each fire, it can be applied to correct emission factors for each pixel. For example, the CO_2 emission factor for a specific biome can be adjusted based on its MCE as higher MCE (VEF) indicates an increase in CO_2 emission factor as the fire burns in

flaming phase emitting larger amounts of CO_2. The advantage of VEF is, it is retrieved from satellite data while the fire is active, appropriate for improving emissions estimations.

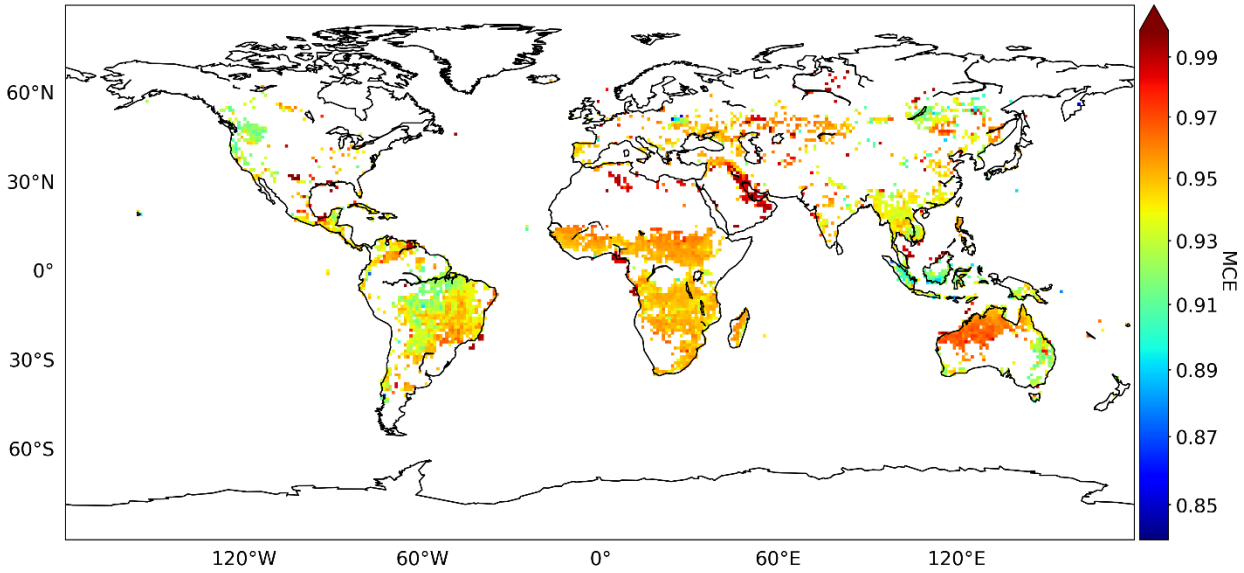

Fig. 11. Global map of MCE for each 1˚ grid which are calculated based on their VEF values for 2015. The Australia shrublands have a high MCE while the forest land cover type areas represent low MCE. The gas flares have the highest MCE.

4.5. Camp Fire

We show the VEF capability in defining the fire combustion phase in Camp fire case study and calculate the fire average MCE for each night. On 8 November 2018, the California deadliest (86 fatalities) and most destructive (US$ 16.5 billion damage) wildfire, was started in Butte County, Northern California. According to the California department of forestry and fire protection reports, the Camp Fire burned an area of around 153,336 acres before it was fully contained on 25 November with the help of the rain. The most intense phase of the fire was in its first four days when the wind speed (22 m/s) facilitated more rapid fire growth which resulted in Camp Fire burning more than 110,000 acres and destroying Paradise town (www.fire.ca.gov).

Camp Fire is an ideal candidate to investigate VEF capability to show the wildfire intensity throughout its lifetime.

As Fig. 12a shows, the VEF (daily-averaged for nighttime fire pixels) is largest (highly flaming) during the first 4 nights of the fire and then starts to reduce. This is consistent with the fact that fire was most destructive in the first four days. The MCE, which was calculated based on equation 9, follows a very similar pattern as VEF. Note that the fire was started on November 8 around 6.33 am local time so the first satellite nighttime observation was on November 9. We show how the fire grew by time for all the nighttime fire pixels in Fig. 12b. Also, we show the VEF has been increased from lower values (November 10) to higher values (November 11) for the fire pixels that are almost in the same areas on the ground (Fig.12 c&d). Fig. S8 shows both VLP and FRP effectively derive VEF for the fire pixels. The change in VEF indicates that the fire grew to a more flaming phase during this 24-hour period which is not observable in the FRP time series indicating of the limited capability of FRP to capture the fire intensity through its lifetime.

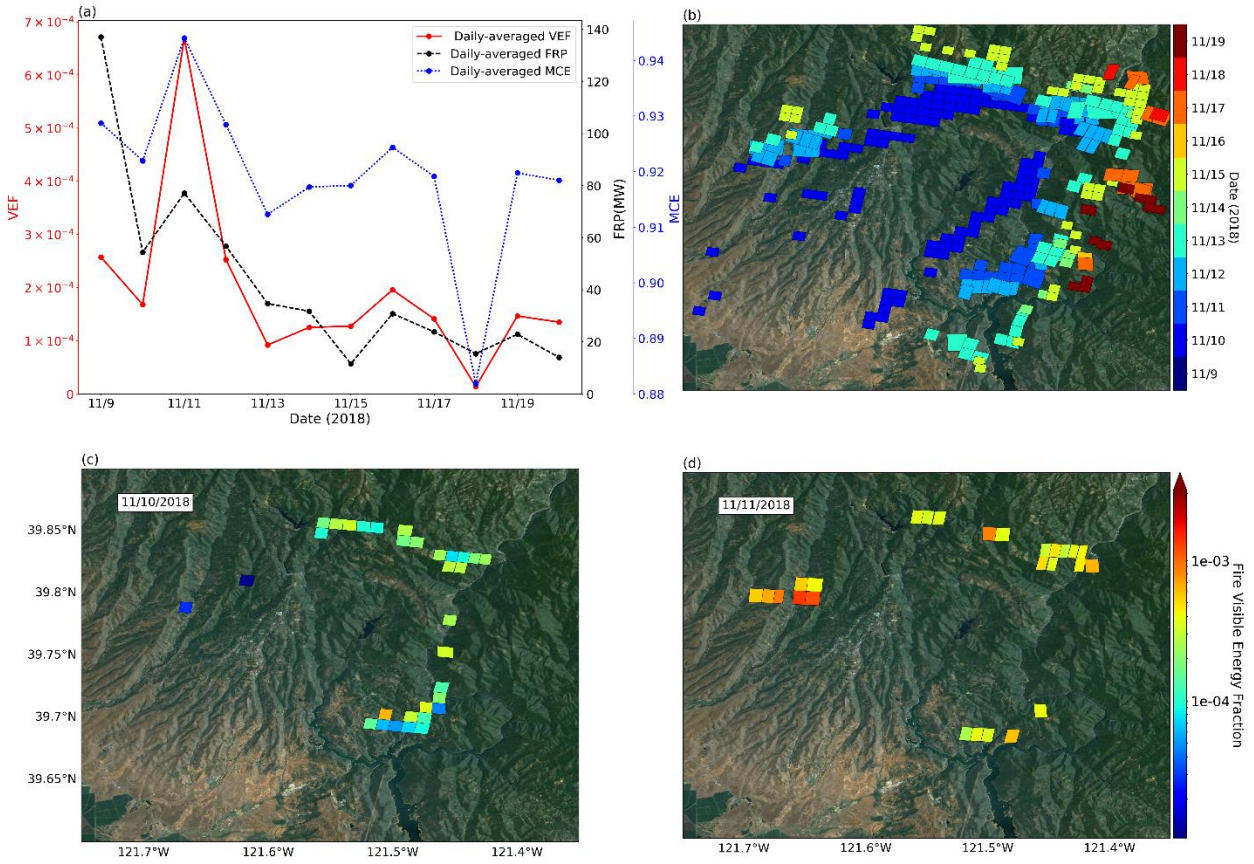

Fig. 12. (a) Time series of FRP (black solid line), VEF (red dashed line), and MCE (green dashed line) derived from the nighttime fire pixels. November 11, 2018 is the peak in the VEF indicating of highly flaming fire phase. (b) The map of all nighttime fire pixels VEF values during the Camp Fire. (c) Observation of Camp Fire intensity on November 10, 2018 when most the fire pixels are in an early stage of their lifetime. (d) Fire intensity increases comparing to the previous day as the fire reaches to a flaming phase on November 11, 2018. Note, the fire pixels for these two days are extracted only from one satellite orbit observation in that day. The background base map is from ESRI (Environmental Systems Research Institute) world imagery service.

CHAPTER 5. CONCLUSIONS

VIIRS DNB provides broadband visible radiance for each pixel. When there is a fire preset in the pixel during the night, this radiance contains information/signal from the flames of the fire (assuming no background contamination). However, VIIRS fire product is based on the M-band (or I-band) which has a different pixel footprint from DNB, and hence the valuable DNB radiance cannot be applied directly to the VIIRS fire pixels. In this study, first, we presented an algorithm for collocating VIIRS DNB radiances to M-band pixel footprint, which makes the hybrid usage of DNB and M-bands data possible. Second, this collocated visible radiance enabled us to develop a ratio representing the visible fraction of the fire energy, which is expected to show a quantitative measure of the fire combustion phase.

The collocation algorithm is based on an accurate area-weighting method. We chose a VIIRS scan near the equator, and divided it into smaller segments before projecting the pixels onto the earth's surface to make the distortion's errors minimum. We implemented the collocation process for each segment separately. The algorithm finds the overlapped DNB pixels both along and across the scan for every M-band pixel, and calculates the corresponding DNB area weights. These weights are stored in a look-up table based on the indices of the pixels. Consequently, taking advantage of the fixed alignment between DNB and M-band pixels in every VIIRS scan, the LUT can be applied to any VIIRS granule across the globe. Also, these DNB area weights provided a reliable criterion to decide whether to keep or exclude an M-band pixel in the case of the redundant M-band pixels which are overlapped from two consecutive scans due to the along-scan pixel growth size. Our results showed that our collocation method is more reliable than the famous nearest-neighbor method as our method results in a much higher correlation between the collocated

DNB radiances and the corresponding M-band pixels $BT4^4$ (the fire pixel energy) values for the 852 nighttime VIIRS fire pixels from California Thomas fire.

We used the resampled DNB radiance to develop the parameter visible light power (VLP). The VLP is the energy from fire flames for each pixel during the night, and its ratio by FRP yields visible energy fraction (VEF) of the pixel. VEF theoretically should be able to show a quantitative measure of the fire combustion phase (smoldering/flaming). The uncertainty sources in VEF include background contamination (e.g. moon effect and city lights) and light attenuation by thick smoke plumes. Although the moon effect is small, intense city lights and thick smoke plume can result in overestimation and underestimation of VEF respectively. Our results demonstrated how VEF successfully characterizes mean-state (annual-averaged) combustion phase of fires based on their fuel (vegetation) type at a pixel and grid level. For example, VEF values for gas flares are distributed in a higher range comparing to other land cover types while the FRP values for all the land cover types (including gas flares) are similarly distributed. An initial assessment of VEF showed that annual-averaged VEF is highly correlated to the mean-state MCE (derived from GFED data) for the general biomes used by GFED. This suggests that the VEF can be used to predict the GFED-based MCE which is a step forward towards enhancing emission estimation for each fire uniquely based on that fire characteristics. For example, we applied VEF to calculate GFED-based MCE for a real wildfire (Camp Fire) at a pixel level. Overall, this study demonstrated the theoretical development of VEF and its potential to measure the fire combustion phase. The results of this work encourage further research to be focused on the application of VEF to enhance the EFs at a pixel level. For example, VEF can be linked to in situ MCE at a pixel level upon the availability of data from different field campaigns which are specifically designated for the VIIRS.

REFERENCES

Akagi, S.K., Yokelson, R.J., Wiedinmyer, C., Alvarado, M.J., Reid, J.S., Karl, T., Crounse, J.D., & Wennberg, P.O. (2011). Emission factors for open and domestic biomass burning for use in atmospheric models. *Atmos. Chem. Phys., 11*, 4039-4072

Andreae, M.O., & Merlet, P. (2001). Emission of trace gases and aerosols from biomass burning. *Global Biogeochemical Cycles, 15*, 955-966

Csiszar, I., Schroeder, W., Giglio, L., Ellicott, E., Vadrevu, K.P., Justice, C.O., & Wind, B. (2014). Active fires from the Suomi NPP Visible Infrared Imaging Radiometer Suite: Product status and first evaluation results. *Journal of Geophysical Research: Atmospheres, 119*, 2013JD020453

Dozier, J. (1981). A Method for Satellite Identification of Surface-Temperature Fields of Subpixel Resolution. *Remote Sensing of Environment, 11*, 221-229

Elvidge, C.D., Kroehl, H.W., Kihn, E.A., Baugh, K.E., Davis, E.R., & Hao, W.M. (1996). *Algorithm for the retrieval of fire pixels from DMSP operational linescan system data. In J. S. Levine (Ed.), Biomass burning and global change: Remote sensing, modeling and inventory development, and biomass burning in Africa*. Cambridge (Massachusetts): MIT Press

Elvidge, C.D., Zhizhin, M., Hsu, F.C., & Baugh, K.E. (2013). VIIRS Nightfire: Satellite Pyrometry at Night. *Remote Sensing, 5*, 4423-4449

Feng, Z., Jun, W., Charles, I., Edward, J.H., Zhifeng, Y., Cui, G., Shenjian, S., Xiaoyang, Z., Shobha, K., Johannes, W.K., Christine, W., & Arlindo da, S. (2014). Sensitivity of mesoscale modeling of smoke direct radiative effect to the emission inventory: a case study in northern sub-Saharan African region. *Environmental Research Letters, 9*, 075002

Ferek, R.J., Reid, J.S., Hobbs, P.V., Blake, D.R., & Liousse, C. (1998). Emission factors of hydrocarbons, halocarbons, trace gases and particles from biomass burning in Brazil. *Journal of Geophysical Research: Atmospheres, 103*, 32107-32118

Ge, C., Wang, J., & Reid, J.S. (2014). Mesoscale modeling of smoke transport over the Southeast Asian Maritime Continent: coupling of smoke direct radiative effect below and above the low-level clouds. *Atmos. Chem. Phys., 14*, 159-174

Giglio, L., Descloitres, J., Justice, C.O., & Kaufman, Y.J. (2003). An Enhanced Contextual Fire Detection Algorithm for MODIS. *Remote Sensing of Environment, 87*, 273-282

Giglio, L., Kendall, J.D., & Justice, C.O. (1999). Evaluation of global fire detection algorithms using simulated AVHRR infrared data. *International Journal of Remote Sensing, 20*, 1947-1985

Giglio, L., Kendall, J.D., & Tucker, C.J. (2000). Remote sensing of fires with the TRMM VIRS. *International Journal of Remote Sensing, 21*, 203-207

Giglio, L., Randerson, J., & van der Werf, G.R. (2013). Analysis of daily, monthly, and annual burned area using the fourth-generation global fire emissions database (GFED4). *Journal of Geophysical Research: Biogeosciences, 118*, 317-328

Giglio, L., Schroeder, W., & Justice, C.O. (2016). The collection 6 MODIS active fire detection algorithm and fire products. *Remote Sensing of Environment, 178*, 31-41

Ichoku, C., & Ellison, L. (2014). Global top-down smoke-aerosol emissions estimation using satellite fire radiative power measurements. *Atmos. Chem. Phys., 14*, 6643-6667

Ichoku, C., & Kaufman, Y.J. (2005). A method to derive smoke emission rates from MODIS fire radiative energy measurements. *IEEE Transactions on Geoscience and Remote Sensing, 43*, 2636-2649

Justice, C.O., Giglio, L., Korontzi, S., Owens, J., Morisette, J.T., Roy, D., Descloitres, J., Alleaume, S., Petitcolin, F., & Kaufman, Y. (2002). The MODIS fire products. *Remote Sensing of Environment, 83*, 244-262

Kaufman, Y.J., Fraser, R.S., & Mahoney, R.L. (1991). Fossil Fuel and Biomass Burning Effect on Climate—Heating or Cooling? *Journal of Climate, 4*, 578-588

Kaufman, Y.J., Justice, C.O., Flynn, L.P., Kendall, J.D., Prins, E.M., Giglio, L., Ward, D.E., Menzel, W.P., & Setzer, A.W. (1998). Potential global fire monitoring from EOS-MODIS. *Journal of Geophysical Research: Atmospheres, 103*, 32215-32238

Li, Z., Kaufman, Y., Ithoku, C., Fraser, R., Trishchenko, A., Gilgil, L., Jin, J., & Yu, X. (2001). A review of AVHRR-based fire active fire detection algorithm: Principles, limitations, and recommendations. In F. Ahern, J.G. Goldammer, & C. Justice (Eds.), *Global and Regional Vegetation Fire Monitoring from Space, Planning and Coordinated International Effort* (pp. 199-225)

Li, Z., Nadon, S., & Cihlar, J. (2000). Satellite-based detection of Canadian boreal forest fires: Development and application of the algorithm. *International Journal of Remote Sensing, 21*, 3057-3069

Mota, B.W., Pereira, J.M.C., Oom, D., Vasconcelos, M.J.P., & Schultz, M. (2006). Screening the ESA ATSR-2 World Fire Atlas (1997–2002). *Atmos. Chem. Phys., 6*, 1409-1424
Ohlemiller, T.J. (1985). Modeling of smoldering combustion propagation. *Progress in Energy and Combustion Science, 11*, 277-310

Penner, J.E., Dickinson, R.E., & O'Neill, C.A. (1992). Effects of Aerosol from Biomass Burning on the Global Radiation Budget. *Science, 256*, 1432-1434

Polivka, T.N., Wang, J., Ellison, L.T., Hyer, E.J., & Ichoku, C.M. (2016). Improving Nocturnal Fire Detection With the VIIRS Day-Night Band. *IEEE Transactions on Geoscience and Remote Sensing, 54*, 5503-5519

Prins, E.M., & Menzel, W.P. (1992). Geostationary satellite detection of bio mass burning in South America. *International Journal of Remote Sensing, 13*, 2783-2799

Prins, E.M., & Menzel, W.P. (1994). Trends in South American biomass burning detected with the GOES visible infrared spin scan radiometer atmospheric sounder from 1983 to 1991. *Journal of Geophysical Research: Atmospheres, 99*, 16719-16735

Ramanathan, V., & Carmichael, G. (2008). Global and regional climate changes due to black carbon. *Nature Geoscience, 1*, 221

Reid, J.S., Koppmann, R., Eck, T.F., & Eleuterio, D.P. (2005). A review of biomass burning emissions part II: intensive physical properties of biomass burning particles. *Atmos. Chem. Phys., 5*, 799-825

Rein, G. (2009). Smouldering Combustion Phenomena in Science and Technology. *International Review of Chemical Engineering, 1*, 3-18

Roberts, G., Wooster, M.J., Perry, G.L.W., Drake, N., Rebelo, L.M., & Dipotso, F. (2005). Retrieval of biomass combustion rates and totals from fire radiative power observations: Application to southern Africa using geostationary SEVIRI imagery. *Journal of Geophysical Research: Atmospheres, 110*

Roberts, G.J., & Wooster, M.J. (2008). Fire Detection and Fire Characterization Over Africa Using Meteosat SEVIRI. *IEEE Transactions on Geoscience and Remote Sensing, 46*, 1200-1218

Sato, T., Kunitomo, T., Yoshii, S., & Hashimoto, T. (1969). On the Monochromatic Distribution of the Radiation from the Luminous Flame. *Bulletin of JSME, 12*, 1135-1143

Schroeder, W., Oliva, P., Giglio, L., & Csiszar, I.A. (2014). The New VIIRS 375m active fire detection data product: Algorithm description and initial assessment. *Remote Sensing of Environment, 143*, 85-96

van Leeuwen, T.T., & van der Werf, G.R. (2011). Spatial and temporal variability in the ratio of trace gases emitted from biomass burning. *Atmos. Chem. Phys., 11*, 3611-3629

Wang, J., & Christopher, S.A. (2006). Mesoscale modeling of Central American smoke transport to the United States: 2. Smoke radiative impact on regional surface energy budget and boundary layer evolution. *Journal of Geophysical Research: Atmospheres, 111*

Ward, D.E., & Hardy, C.C. (1991). Smoke emissions from wildland fires. *Environment International, 17*, 117-134

Yokelson, R.J., Griffith, D.W.T., & Ward, D.E. (1996). Open-path Fourier transform infrared studies of large-scale laboratory biomass fires. *Journal of Geophysical Research: Atmospheres, 101*, 21067-21080

APPENDIX

A.1. Collocation look-up table

Once the collocation and bow-tie effect detection are completed, we store the results in a look-up. M-band scan is a 2-dimensional array of pixels with 16 rows and 3200 columns. We ravel this 2-dimensional array to a 1-dimensional array yielding an array with 16×3200 elements with every sixteen elements corresponds to a row in the 2-dimensional array. Also, we ravel the 2-dimensional pixel array of the DNB scan zone to a 1-dimensional array starting from 1 to 16×4064. In this way, we can use the 1-dimensional array values (1 to 16×4064) to denote the collocated DNB indices for each M-band pixel. There are four variables stored in the look-up table. First variable called "Collocated_DNB_Indices" which is a 2-dimensional array with 12 rows and 16×3200 columns. Each value is a number from 1 to 16×4064 corresponding to the indices of DNB pixels. Every 3200 columns in each row represent a row in the 2-dimensional array of unraveled M-band pixels. Also, the 12 rows in Collocated_DNB_Indices array denotes the maximum number of DNB pixels that can overlap a single M-band pixel. Fig. 2b shows near the edge of the scan zone 12 DNB pixels cover a single M-band pixel. As a result, each M-band pixel can have 12 or less DNB pixels collocated to it. Hence, if an M-band pixel has 10 collocated DNB pixels, 10 rows will contain values and the other two will be set as zero. The second look-up table variable "DNB_Weights" is an array with the same dimension as "Collocated_DNB_Indices", but the elements represents the weight (0 to 1) for each collocated DNB pixel. The third variable "M-band_Overlapped" is a 2-dimensional array with the same dimension as the M-band scan zone (16×3200). In this array the overlapped pixels have the value of -999.7 while all the other pixels have the fixed value 1. The last variable which is called "M-band_Areas" is a 2-dimensional array (16×3200) with each element containing the area for the corresponding M-band pixel in m^2.

A.2. Tables

Table A1. VIIRS bands spectral characteristic.

Band	Spectral Range (µm)	Central Wavelength (µm)
M1	0.402 - 0.422	0.412
M2	0.436 - 0.454	0.445
M3	0.478 - 0.488	0.488
M4	0.545 - 0.565	0.555
M5	0.662 - 0.682	0.672
M6	0.739 - 0.754	0.746
M7	0.846 - 0.885	0.865
M8	1.23 - 1.25	1.240
M9	1.371 - 1.386	1.378
M10	1.58 - 1.64	1.61
M11	2.23 - 2.28	2.25
M12	3.61 - 3.79	3.7
M13	3.97 - 4.13	4.05
M14	8.4 - 8.7	8.55
M15	10.26 - 11.26	10.763
M16	11.54 - 12.49	12.013
I1	0.6 - 0.8	0.64
I2	0.85 - 0.88	0.865
I3	1.58 - 1.64	1.61
I4	3.55 - 3.93	3.74
I5	10.5 - 12.4	11.45
DNB	0.5 - 0.9	0.7

Table A2. VIIRS M-band aggregation scheme (from left end of the scan to the nadir).

Aggregation zones from nadir	Samples aggregated per pixel		M-band pixel Index[1] range
	Along scan	Across scan	
1	3	1	1:640
2	2	1	641:1008
3	1	1	1009:1600

[1] The M-band pixel index in each scan line starts from 1 (left side of the scan) and ends at 3200 (right side of the scan)

Table A3. VIIRS DNB aggregation scheme (from left end of the scan to the nadir).

Aggregation zones from nadir	Samples aggregated per pixel		DNB pixel index[2] range
	Along scan	Across scan	
1	66	42	1848:2032
2	64	42	1776:1847
3	62	41	1688:1775
4	59	40	1616:1687
5	55	39	1536:1615
6	52	38	1464:1535
7	49	37	1400:1463
8	46	36	1336:1399
9	43	35	1272:1335
10	40	34	1208:1271
11	38	33	1144:1207
12	35	32	1064:1143
13	33	31	1008:1063
14	30	30	928:1007
15	28	29	857:928
16	26	28	785:856
17	24	27	713:784
18	23	27	681:712
19	22	26	633:680
20	21	26	601:632
21	20	25	553:600
22	19	25	513:552
23	18	24	457:512
24	17	24	417:456

Table A3 - continued

25	16	23	345:416
26	15	23	321:344
27	15	22	289:320
28	14	22	225:288
29	13	21	161:224
30	12	21	97:160
31	12	20	81:96
32	11	20	1:80

[2] The DNB pixel index in each scan line starts from 1 (left side of the scan) and ends at 4064 (right side of the scan).

Table A4. VIIRS DNB to M-band collocating segments (from left end of the scan to right end).

Collocation segment	DNB pixel index range	M-band pixel index range
1	1:97	1:44
2	97:224	45:112
3	224:320	113:172
4	320:417	173:238
5	417:512	239:311
6	512:601	312:386
7	601:681	387:462
8	681:785	463:569
9	785:857	570:645
10	857:929	646:689
11	929:1009	690:741
12	1009:1065	742:781
13	1065:1115	782:842
14	1145:1209	843:895
15	1209:1273	896:951
16	1273:1337	952:1010
17	1337:1402	1011:1053
18	1402:1465	1054:1098
19	1465:1537	1099:1152
20	1537:1617	1153:1216
21	1617:1689	1217:1278
22	1689:1777	1279:1357
23	1777:2033	1358:1600
24	2033:2288	1601:1841
25	2288:2376	1842:1980
26	2376:2448	1921:1982

Table A4 - continued

27	2448:2528	1983:2046
28	2528:2600	2047:2100
29	2600:2665	2101:2146
30	2665:2728	2147:2188
31	2728:2792	2189:2246
32	2792:2856	2247:2302
33	2856:2920	2303:2355
34	2920:3000	2356:2416
35	3000:3056	2417:2456
36	3056:3136	2457:2508
37	3136:3208	2509:2552
38	3208:3280	2553:2625
39	3280:3384	2626:2733
40	3384:3464	2734:2808
41	3464:3553	2809:2883
42	3553:3648	2884:2996
43	3648:3744	2957:3022
44	3744:3841	3023:3082
45	3841:3968	3083:3151
46	3968:4064	3152:3200

Table A5. Simulated VEFs for different temperatures with a uniform background aerosol optical depth around 0.1 (smoke particles) using UNL-VRTM.

Fire Temperature (k)	VEF
400	2.06×10^{-13}
500	1.31×10^{-10}
600	1.04×10^{-8}
700	2.46×10^{-7}
800	2.68×10^{-6}
900	1.75×10^{-5}
1000	7.93×10^{-5}
1100	2.75×10^{-4}
1200	7.84×10^{-4}
1300	1.91×10^{-3}
1400	4.11×10^{-3}
1500	8.04×10^{-3}
1600	1.44×10^{-2}
1700	2.44×10^{-2}
1800	3.89×10^{-2}
1900	5.91×10^{-2}
2000	8.63×10^{-2}
2100	1.21×10^{-1}
2200	1.66×10^{-1}
2300	2.22×10^{-1}
2400	2.89×10^{-1}

Table A6. Annual-averaged VEF for different biomes and gas flares.

Biome	VEF
Evergreen needleleaf forest	1.74×10^{-4}
Evergreen broadleaf forest	3.65×10^{-4}
Deciduous needleleaf forest	1.68×10^{-3}
Deciduous broadleaf forest	4.74×10^{-4}
Mixed forest (MF)	1.19×10^{-3}
Closed shrublands	1.02×10^{-3}
Open shrublands	2.33×10^{-3}
Woody savannas	5.11×10^{-4}
Savannas	8.86×10^{-4}
Grasslands	1.38×10^{-3}
Croplands	1.25×10^{-3}
Cropland/Natural vegetation mosaic	1.80×10^{-3}
Peatland	4.42×10^{-5}
Gas Flare	1.07×10^{-2}

A.2. Figures

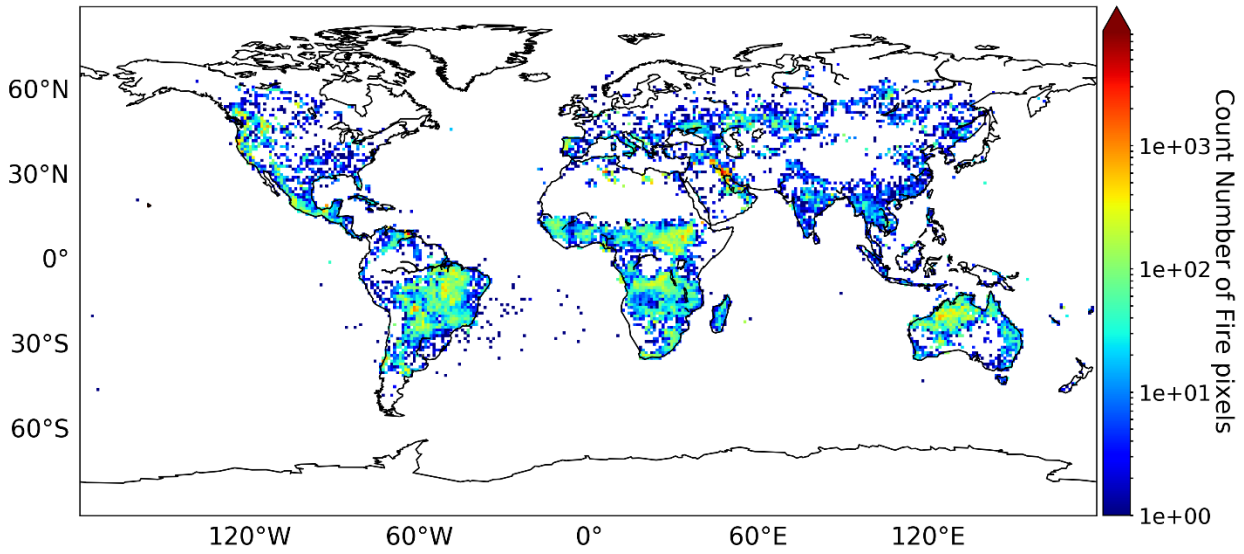

Fig. A1. Global map of VIIRS AF nighttime fire pixels for 2017. Each 1˚ grid represents the count number of fire pixels.

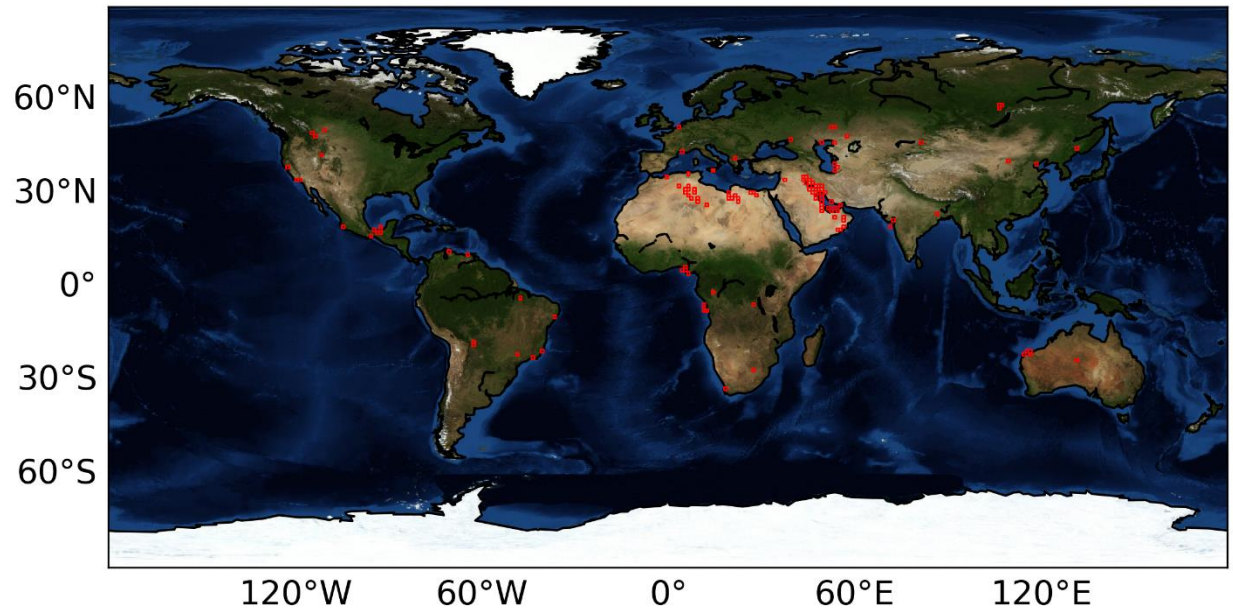

Fig. A2. Global map of gas flares used in this study. The background base map is from ESRI (Environmental Systems Research Institute) world imagery service.

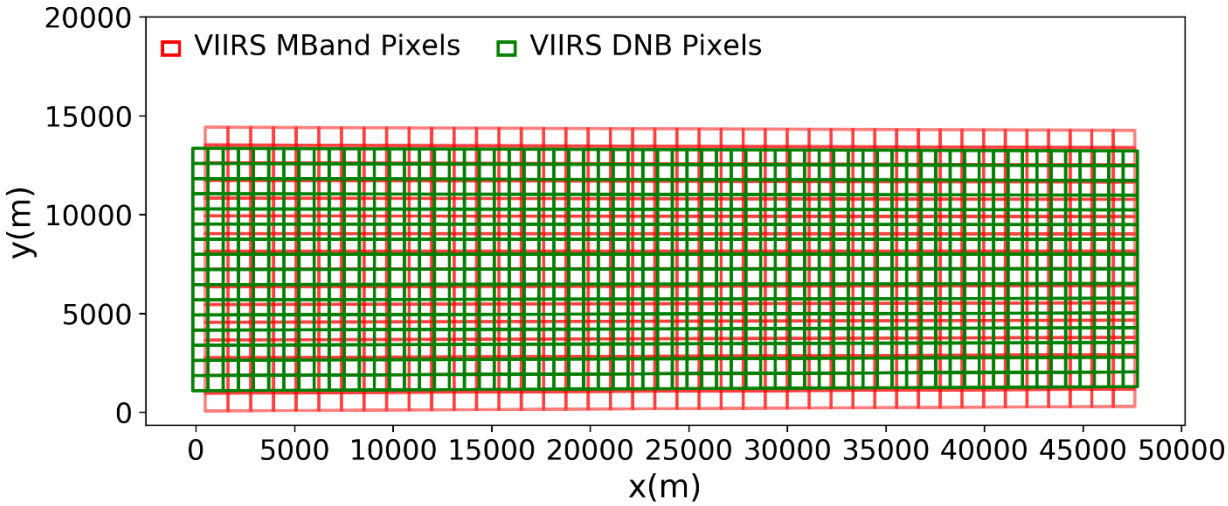

Fig. A3. Collocation segment 7 consists of projected DNB (green pixels) and M-band pixels (red).

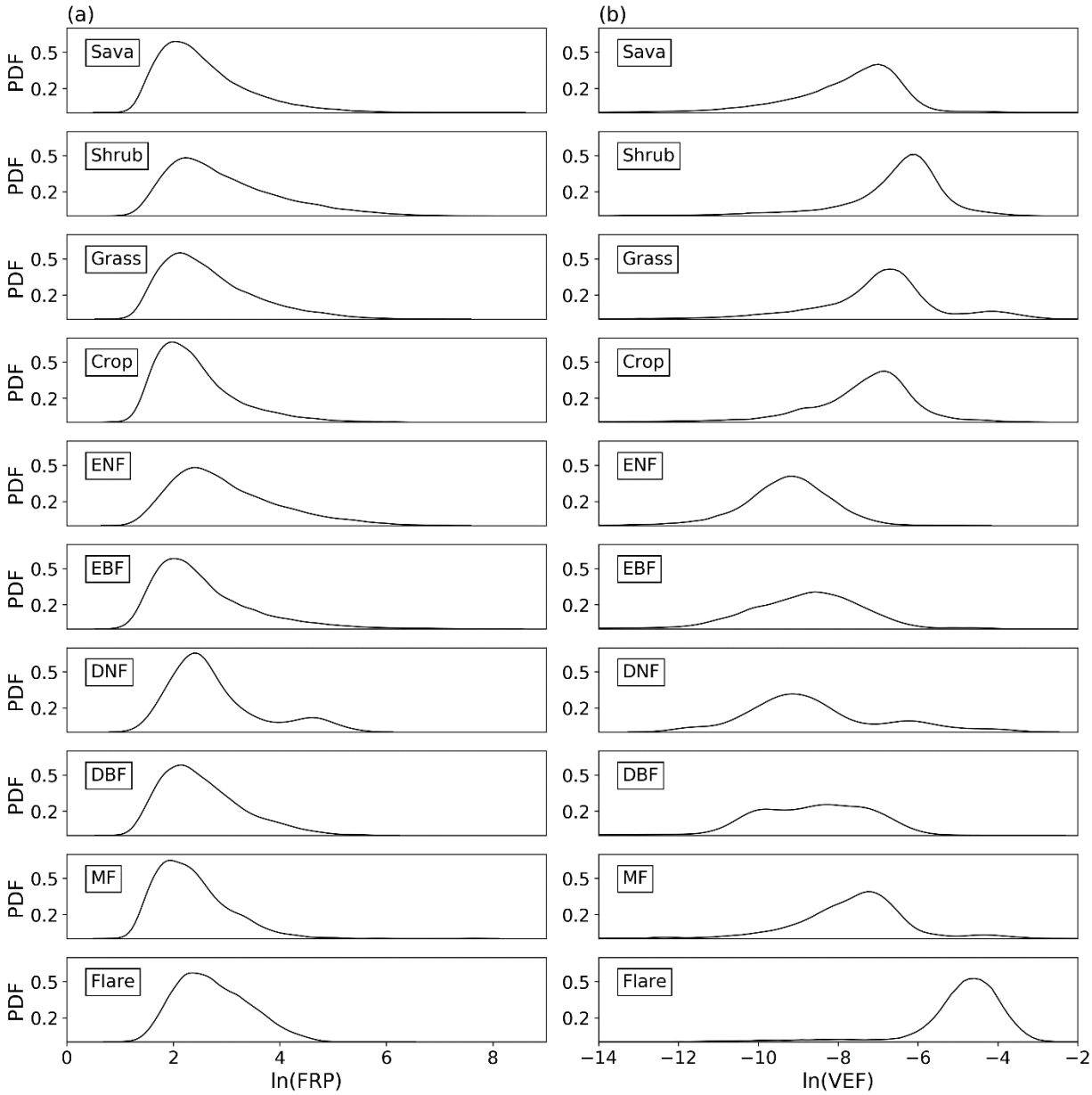

Fig. A4. The probability density functions (PDF) for different vegetation types showing their VEF and FRP distributions (at the pixel level) for the year 2017. The distribution of FRP is similar for almost all of the fire types while VEF distinguished different vegetation types.

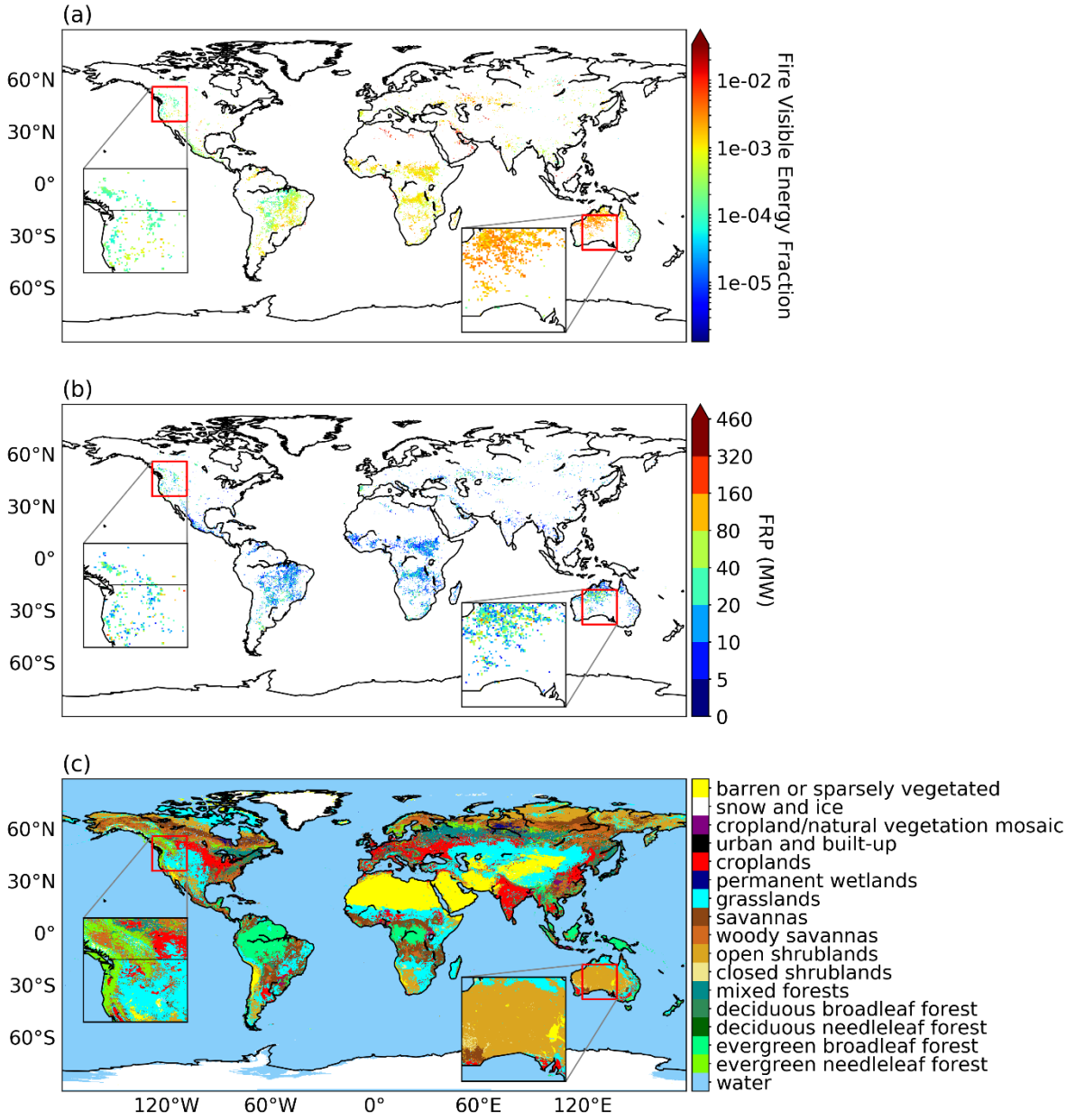

Fig. A5. (a) Global map of VEF for 2017. Each 0.25˚ grid represents the average VEF value for the year 2017. The VEF map shows the transition from forest land cover type in North America (lower VEF) to shrublands in Australia (higher VEF). The red grids (highest VEF) are mostly corresponding to the gas flares while the lowest VEF (blue color) are where the evergreen forests are. There are no detected nighttime fire pixels in polar regions including Greenland and Alaska due to the long day length (more than 20 hours) during their fire seasons in summer. (b) Global map of FRP for 2017. Each 0.25˚ grid represents the average nighttime FRP value for the year 2017. The FRP map is not capturing the fire combustion phase differences based on the land cover type as the FRP spread for shrubland and forest are similar. (c) Global landcover map generated based on the MODIS Land Cover Type Climate Modeling Grid for year 2017. The land cover categories are according to IGBP scheme.

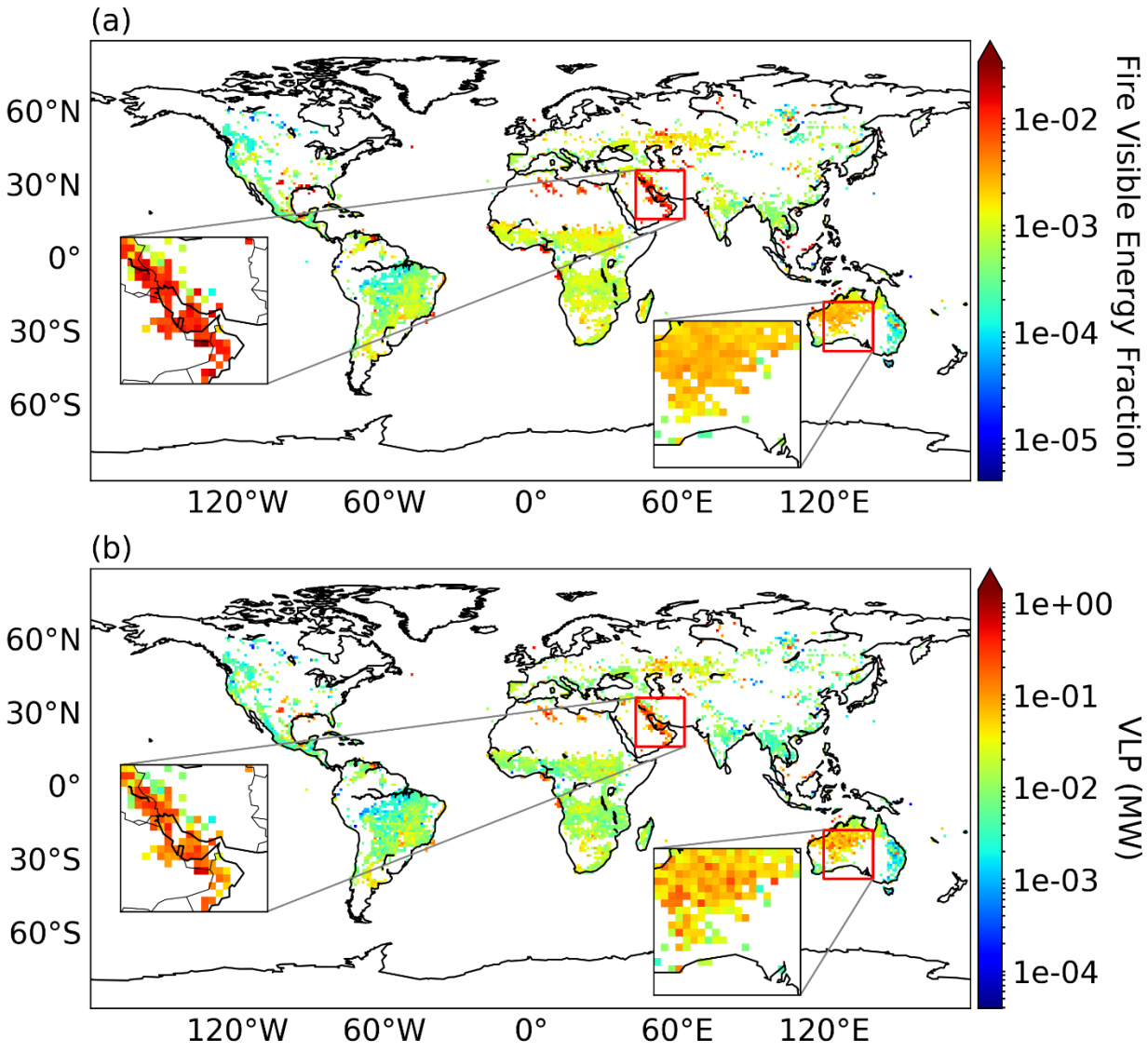

Fig. A6. (a) Global map of VEF for 2017. Each 1˚ grid represents the average VEF value for the year 2017. The VEF map shows the separation between gas flares in Middle East and shrublands in Australia. (b) Global map of VLP for 2017. Each 1˚ grid represents the average nighttime VLP value for the year 2017. Although the VLP is showing to be the main driver of mean-state VEF for each grid, the gas flares are better distinguished in VEF map as it is not driven by fire size unlike VLP.

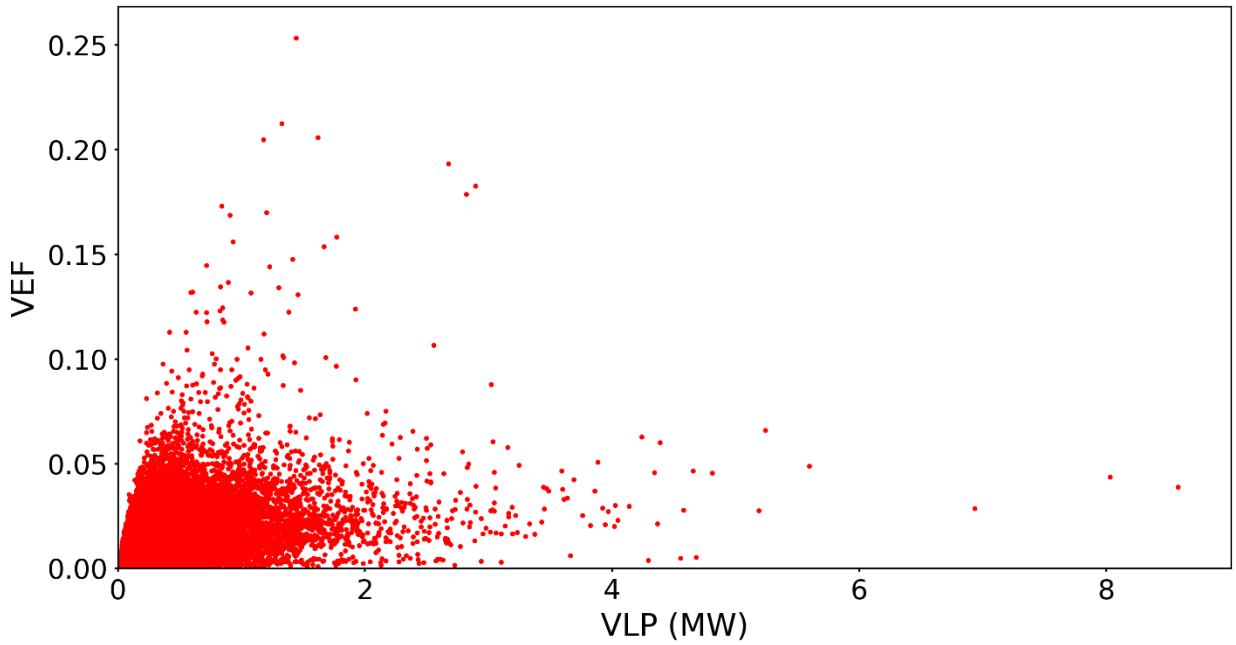

Fig. A7. Scatter plot of VEF and VLP (MW) for VIIRS AF (nighttime) fire pixels for 2017. There are pixels with very large VEF (e.g. more than 0.2), but not large VLP. These fire pixels are from gas flares in Venezuela indicating that VEF is capable of distinguishing between small flaming fires and large smoldering fires.

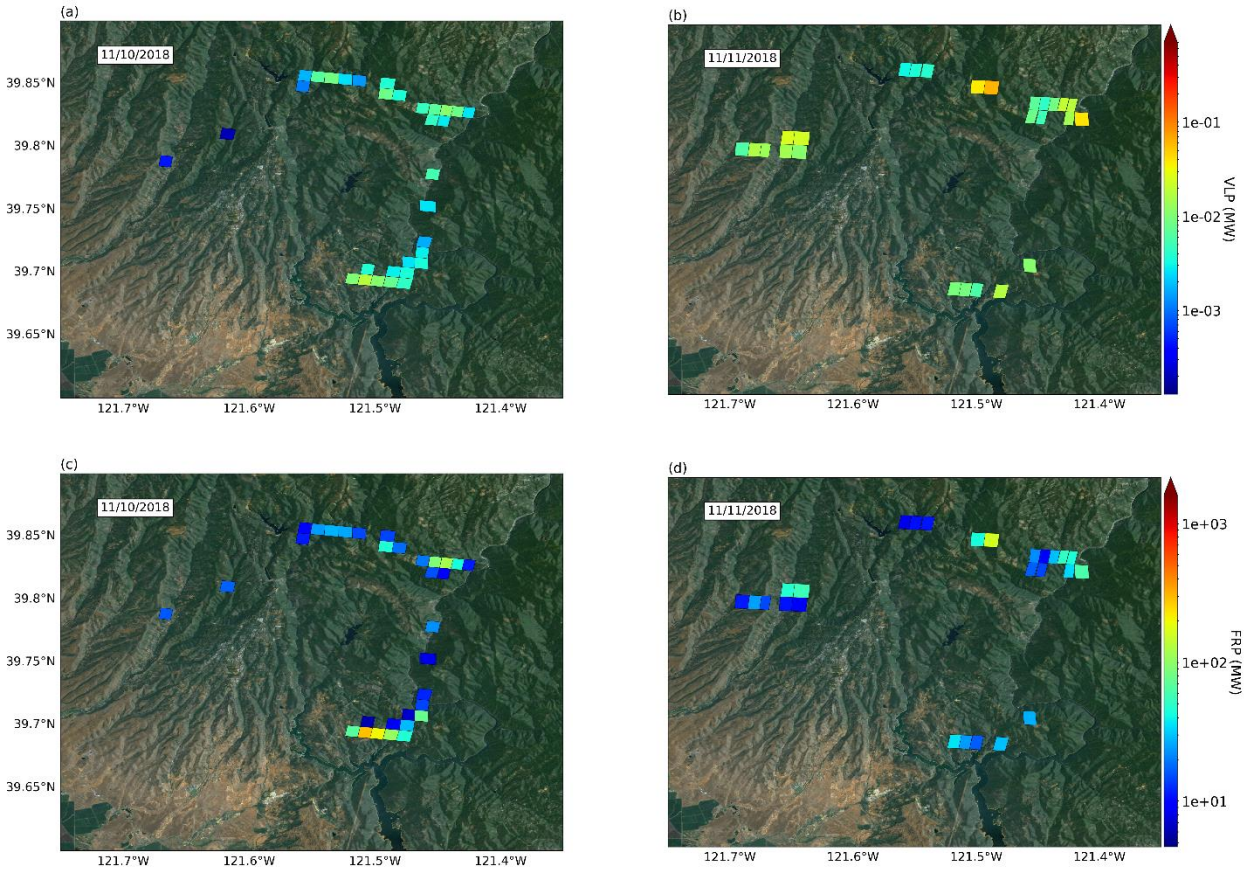

Fig. A8. (a) Observation of Camp Fire visible energy on November 10, 2018. (b) Fire VLP increases comparing to the previous day as the fire reaches to a flaming phase on November 11, 2018. (c) The map of Camp Fire nighttime fire pixels FRP values on November 10, 2018. Note how high FRP, which can be due to the large fire size, derive VEF (Fig. 12c) of the fire pixels. (d) Observation of Camp Fire FRP on November 11, 2018. Note, the fire pixels for these two days are extracted only from one satellite orbit observation in that day. The background base map is from ESRI (Environmental Systems Research Institute) world imagery service.